Direct Numerical Simulations of Type Ia Supernovae Flames II: The Rayleigh-Taylor Instability

J. B. Bell[1], M. S. Day[1], C. A. Rendleman[1], S. E. Woosley[2], M. Zingale[2]

ABSTRACT

A Type Ia supernova explosion likely begins as a nuclear runaway near the center of a carbon-oxygen white dwarf. The outward propagating flame is unstable to the Landau-Darrieus, Rayleigh-Taylor, and Kelvin-Helmholtz instabilities, which serve to accelerate it to a large fraction of the speed of sound. We investigate the Rayleigh-Taylor unstable flame at the transition from the flamelet regime to the distributed-burning regime, around densities of 10^7 g cm^{-3}, through detailed, fully resolved simulations. A low Mach number, adaptive mesh hydrodynamics code is used to achieve the necessary resolution and long time scales. As the density is varied, we see a fundamental change in the character of the burning—at the low end of the density range the Rayleigh-Taylor instability dominates the burning, whereas at the high end the burning suppresses the instability. In all cases, significant acceleration of the flame is observed, limited only by the size of the domain we are able to study. We discuss the implications of these results on the potential for a deflagration to detonation transition.

Subject headings: supernovae: general — white dwarfs — hydrodynamics — nuclear reactions, nucleosynthesis, abundances — conduction — methods: numerical

1. INTRODUCTION

Accelerating a thermonuclear flame to a large fraction of the speed of sound (possibly supersonic) is one of the main difficulties in modeling Type Ia supernovae (see the recent review by Hillebrandt & Niemeyer 2000 and references therein). Numerical results have shown that a prompt detonation does not yield the right abundance pattern to account for the

---

[1]Center for Computational Science and Engineering, Lawrence Berkeley National Laboratory, Berkeley, CA 94720

[2]Dept. of Astronomy & Astrophysics, The University of California, Santa Cruz, Santa Cruz, CA 95064

observations (Arnett et al. 1971); consequently, the burning must begin as a subsonic flame. One dimensional simulations show that the flame needs to reach approximately one third of the speed of sound to properly account for the explosion energetics and nucleosynthetic yields (Woosley et al. 1984; Nomoto et al. 1984), although, a transition from a deflagration to a detonation at some late stage of the explosion (Khokhlov 1991; Niemeyer & Woosley 1997) is not ruled out. Laminar flame speeds are too slow by several orders of magnitude (Timmes & Woosley 1992), so instabilities and the interaction with flame-generated turbulence are turned to in hopes of providing a mechanism to considerably accelerate the flame.

In this paper, we focus on the effects of the Rayleigh-Taylor (RT) instability (Taylor 1950; Chandrasekhar 1981) on the flame. After ignition, the subsonic flame moves outward from the center of the star. The pressure is essentially continuous across the flame. Furthermore, since the star has time to expand in response to the burning, this pressure also remains constant in time. As the flame propagates, it leaves behind hot ash that is less dense than the cool fuel. Gravity points toward the center of the star, so this flame front is RT unstable. Bubbles of hot ash will rise and try to exchange places with spikes of cool fuel, increasing the surface area of the flame and leading to an enhancement of the flame speed. It is possible that this acceleration, operating on the stellar scale, can bring the flame speed up to a significant fraction of the speed of sound. Furthermore, the shear layer between the fuel and ash which develops as the instability evolves is Kelvin-Helmholtz unstable, creating turbulence in the region of the flame. As the flame surface is wrinkled by the RT instability, it will interact with this turbulence. We look in detail at the interaction between the RT instability and the flame on small scales through 2-dimensional spatially resolved simulations in conditions appropriate to the late stages of a Type Ia supernova explosion.

The difference in scale between the white dwarf and the flame width is enormous (up to 12 orders of magnitude), making direct numerical simulations of the whole explosion process impossible. Nevertheless, simulations of RT unstable flames have been attempted for some time, both on the full stellar scale and as smaller, constant density micro-physical studies. Various techniques and approximations are used to follow an unresolved flame on these scales. Some of the earliest such calculations (Müller & Arnett 1982, 1986) used donor-cell advection to follow a combustion front through the star, burning most of it, and releasing enough energy to produce an explosion. In their model, the flame was propagated essentially through numerical diffusion. The RT instability was resolved only on the very largest scales of the star, missing the turbulence generated on the small scales. Livne (1993) used a two-dimensional implicit Lagrangian-remap hydrodynamics code with a mixing-length subgrid model to follow a RT unstable flame. The diffusion of reactants in the Lagrangian-remap scheme is much lower than that used in Müller & Arnett (1982, 1986), so a more physical flame speed could be used. The flame speed was chosen to be either the conductive (laminar)

or turbulent speed—which ever was larger. Again, the whole star was modeled, with coarse resolution, showing that the RT instability sets up and greatly convolutes the flame front, but the resulting acceleration left the flame too slow to match observations. Livne (1993) suggested that more resolution is needed to get the small scale physics right.

The effects of turbulence on the burning were investigated by Niemeyer & Hillebrandt (1995b); Khokhlov (1995). Two-dimensional, small scale RT simulations using a thickened-flame model, coupled to an explicit Lagrange-remap PPM (Colella & Woodward 1984) implementation to model a thin flame front were performed by Khokhlov (1993) and later extended to 3-d (Khokhlov 1994). In this model, a reaction-diffusion equation for the fuel concentration is solved along with the Euler equations, with the conductivity and reaction rate modified to yield the desired laminar flame speed and a flame that was a few computational zones wide. The thermal structure of the true flame is stretched greatly, and, as a result, curvature effects of the flame are not properly included. Energy is deposited behind the flame to couple this reaction-diffusion model to the hydrodynamics. Similar techniques have also been used for terrestrial flames (see for example O'Rourke & Bracco 1979). Simulations of the RT instability at a density of 10^8 g cm^{-3} lead the author to conclude that while the flame accelerates, it is too small of an acceleration (when scaled up to the size of the star) to account for the observations, and that a deflagration-detonation transition may be more promising. Owing to the difference in behavior between two-dimensional and three-dimensional turbulence, Khokhlov (1994) concludes that the turbulence was more effective in increasing the flame speed in 3-d. Khokhlov (1995) demonstrated scaling relations for the 3-d RT unstable flame and concluded that the turbulent flame speed does not depend on the small scale burning or the laminar flame speed.

The independence of the turbulent flame speed on the laminar speed was also postulated by Niemeyer & Hillebrandt (1995b), who performed a full-stellar model based on Kolmogorov scaling of turbulence from the large stellar scales down to the flame scales. Here, a turbulent scaling model using the Gibson length (the scale at which an eddy is completely burned during a single turnover) as the small scale cutoff yields a turbulent flame velocity prediction for the grid scale. This was coupled with a subgrid model for the turbulent kinetic energy, and implemented within the PPM algorithm. Their simulations of the flame propagating through the whole star showed the RT instability dominating the flow, but the flame did not accelerate enough to produce an explosion.

More recently, large scale simulations of pure deflagration explosion have been performed using two different methods, level-sets (Reinecke et al. 1999a,b, 2002) and a thickened-flame model (Gamezo et al. 2003) with a Sharp-Wheeler (Sharp 1984; Glimm & Li 1988) RT subgrid model. Both groups using PPM as their underlying explicit hydrodynamics method.

Different numbers and locations of the ignition points are used, but the 3-d simulations by both groups release enough energy to explode the star, with the burning proceeding solely as a deflagration.

These studies have demonstrated the tremendous effect the RT instability has as the dominant acceleration mechanism of the flame—to the point where, in some simulations, a deflagration alone can unbind the star. However, in all the cases discussed above, some model for the flame or turbulence on scales smaller than the grid resolution was required. In this paper, we present fully resolved simulations of RT unstable flames at the densities appropriate to the late stages of the explosion—no flame model is used. Fully resolving the flame means that the effects of curvature and strain on the flame are implicitly accounted for. Curvature effects on flames in conditions close to those studied here were found to be important in Dursi et al. (2003), where laminar flames were propagated in diverging and converging spherical geometries. Here, the effects can be even larger as the flame will experience sharp kinks as it is distorted by the RT instability. To achieve converged steady-state laminar flames, approximately five grid point resolution in the thermal width is required. This limits the size of the domain that can be modeled significantly (although the adaptive mesh refinement employed here helps greatly), but frees us from the need to deal with subgrid models. Resolved simulations at the smallest scales complement the full star flame-model calculations, and it is hoped that progress from the small scales up will allow us in the future to develop and calibrate more accurate subgrid models.

Fully resolved multidimensional Type Ia-like flame simulations are rare (Niemeyer & Hillebrandt 1995a; Zingale et al. 2001; Bell et al. 2003a), mainly because the flame moves so slowly, requiring excessive numbers of timesteps for compressible codes. Resolved calculations of the reactive RT instability have been performed before (Vladimirova & Rosner 2003), but using model flames (a KPP-type reaction, Kolmogoroff et al. 1937) and a Boussinesq approximation, under conditions that are not directly applicable to Type Ia SNe. When extrapolated to the astrophysical regime, they predict a flame speed independent of the laminar speed, similar to that found by Khokhlov (1995). However, compressibility was neglected in these calculations. Here we use a low Mach number formulation of the equations of motion, which retains the compressibility, but frees us from the restrictive acoustic timestep constraint, and we use realistic input physics (reaction rate, EOS, etc.) appropriate to the conditions in a Type Ia SNe explosion.

Flame instabilities stretch and wrinkle the flame, increasing the bulk burning rate. The SNe flame is subject to a combination of the Landau-Darrieus (Landau 1944; Darrieus 1938) and RT instabilities, as well as the interaction with turbulence. In a previous paper, (Bell et al. 2003a, henceforth referred to as paper I), we looked at Landau-Darrieus unstable

flames, and validated the low Mach number method for astrophysical flames, confirming the results of earlier studies that the acceleration of the laminar flame is quite small, while finding no evidence for the breakdown of the cusps in the non-linear regime. In the present paper, we look in detail at the interaction between the burning and the RT instability. A RT driven flame behaves very differently from its laminar counterpart. Aside from looking at the increase in velocity over the laminar speed the wrinkling provides, we seek to determine whether there is a simple scaling relation that matches these results, and whether such a relation holds over the whole range of densities, where the character of the burning is expected to change dramatically.

In §2, we discuss the effects of the burning on the RT instability when we enter the distributed burning regime. In §3, the low Mach number numerical method and input physics are described, followed by the results of our simulations in §4. We conclude in §5 by discussing the implications of the RT burning process on the explosion mechanism for Type Ia SNe.

2. THE EFFECTS OF BURNING ON THE RAYLEIGH-TAYLOR INSTABILITY

The RT instability has been well studied analytically (Taylor 1950; Layzer 1955; Chandrasekhar 1981) and numerically, both as an incompressible (see recent results by Young et al. 2001; Cook & Dimotakis 2001) and compressible (see for example Glimm & Li 1988; Calder et al. 2002) fluid. In the absence of burning, the growth of the multimode RT instability in the non-linear regime is characterized by two parameters, one describing the terminal velocity, and the other describing bubble merger (Glimm & Li 1988). Bubbles are assumed to merge when the difference in their heights exceeds some critical multiple of the smaller bubble size. This leads to an expression for the average position of the interface,

$$h = \alpha A g t^2 \ , \tag{1}$$

(Sharp 1984) where α is a function of the two parameters, and $A = (\rho_{\mathrm{fuel}} - \rho_{\mathrm{ash}})/(\rho_{\mathrm{fuel}} + \rho_{\mathrm{ash}})$ is the Atwood number. Much theoretical, computational, and experimental work aims to measure α, and some evidence suggests that it may be constant for a wide range of initial conditions (George et al. 2002). The velocity of the merged bubbles can be written as

$$v = c\sqrt{Agh} \ , \tag{2}$$

where $c \sim 1/2$ (Davies & Taylor 1950). These expressions were all formulated for the non-reactive RT instability and studies of rising bubbles. Numerical experiments of reactive

RT instabilities in SNe conditions (Khokhlov 1995) using a thickened-flame model found agreement with the above velocity expression, with $c = 0.5$. Expressions of this form have been used as a subgrid model for the flame speed in full-star, pure deflagration calculations of Type Ia explosions in 1-d (Niemeyer & Woosley 1997) and 3-d (Gamezo et al. 2003), resulting in a successful explosion of the star. These results suggest that the RT instability is the dominant acceleration mechanism for the flame. Given the importance of RT instability to the dynamics of the star, our goal here is to explore reacting RT physics through direct numerical simulations.

The presence of reactions introduces fundamental changes in the dynamics of the RT instability. Woosley (1990) and Timmes & Woosley (1992) argued that, unlike a non-reactive RT instability, where all wavelengths can grow (in the absence of surface tension), burning introduces a small scale cutoff to the instability. The growth rate for the pure RT instability is determined by the dispersion relation

$$\omega^2 = gkA \tag{3}$$

(Chandrasekhar 1981), where ω is the angular frequency and k is the horizontal wave number for the dominant mode. We note that we have ignored contributions due to surface tension. By equating the period for the growth of the instability to the laminar flame propagation timescale, Timmes & Woosley (1992) showed that there is a critical wavelength below which any perturbations will be washed out by burning. This wavelength is called the fire-polishing wavelength, λ_{fp}:

$$\lambda_{\mathrm{fp}} = 4\pi \frac{v_{\mathrm{laminar}}^2}{g_{\mathrm{eff}}} \ , \tag{4}$$

where $g_{\mathrm{eff}} = gA$ is the effective gravitational acceleration. We note that this is a simple estimate, nevertheless, it provides a useful measure of the effectiveness of the RT instability on disrupting the flame.

The suppression of RT growth of wavelengths less than λ_{fp} makes it a critical parameter for studying reacting RT instabilities. Table 1 lists the flame properties, as computed by the code described in §3, including λ_{fp} for the densities we are considering. As the density of the white dwarf decreases, the flame speed decreases sharply while the flame width, l_f, increases. As Table 1 shows, at the densities we are considering, we pass from the regime where $\lambda_{\mathrm{fp}} \ll l_f$ (low densities) to $\lambda_{\mathrm{fp}} \gg l_f$ (high densities). When $\lambda_{\mathrm{fp}} \ll l_f$, the RT instability will dominate the flame, to the point where it may no longer be continuous, and one can not draw a simple curve from one side of the domain to the other marking the flame position. This increase in complexity of the flame surface signifies that we are leaving the flamelet regime.

Niemeyer & Woosley (1997) made estimates of the density where the burning transitions from the flamelet regime to the distributed burning regime, in which a distinguished local

flame surface is not apparent. Using the flame properties tabulated in Timmes & Woosley (1992) and equating the Gibson scale to the flame width, they found that for a 0.5 ^{12}C/ 0.5 ^{16}O flame, the burning will enter the distributed burning regime at a density of 1– 5×10^7 g cm^{-3}. Niemeyer & Kerstein (1997) refined this estimate by suggesting that since the turbulence present in a Type Ia explosion is generated by the RT instability, it should follow Bolgiano-Obukhov rather than Kolmogorov statistics. They found a slightly lower transition density of $\sim 10^7$ g cm^{-3}. At these densities, the turbulence is intense enough to disrupt the flame. We note that this transition density is right in the range where the fire polishing length becomes equal to the flame width, as discussed above.

This density range is also interesting in the context of deflagration to detonation transitions (DDT). Arguments based on nucleosynthesis and one-dimensional modeling suggest that if the burning in a Type Ia supernova were to transition from a deflagration to a detonation, this transition would need to occur at a density around 10^7 g cm^{-3} (see for instance Hoeflich & Khokhlov 1996). The correlation between this DDT density and the density marking the transition to the distributed burning regime was pointed out by Niemeyer & Woosley (1997) and Khokhlov et al. (1997). One-dimensional turbulence studies of the flame-turbulence interaction at these densities were performed by Lisewski et al. (2000), where it was observed that the turbulence disrupts the flame sufficiently in some cases to create local explosions as the hot ash comes in contact with pockets of cool fuel. If these regions of fuel are large enough, these local explosions may be able to initiate a DDT.

Direct numerical simulations of thermonuclear flames at these densities do not exist. Niemeyer et al. (1999) performed simplified flame model calculations in 3-d using a source term relevant to flames in Type Ia supernovae. They concluded that for densities larger than $\sim 10^7$ g cm^{-3}, scaling the flame speed in direct proportion to the increase in surface area is a valid subgrid model. For densities below 10^7 g cm^{-3} however, they state that the effects of turbulence become important.

Together, the flame width and the fire-polishing length set strict limits on the densities and size of domains that can be addressed through fully resolved simulations. Steady state laminar flame simulations show that we need about 5–10 zones inside the flames thermal width,

$$l_f \equiv \frac{T_{\mathrm{ash}} - T_{\mathrm{fuel}}}{\max\{\nabla T\}} \ . \tag{5}$$

We note that this width measurement is a factor of 2–3 narrower than the alternate measure defined as the width of the region where the temperature is 10% above the fuel temperature to 90% of the ash temperature that was used in Timmes & Woosley (1992). In order for the RT instability to develop, we need the computational domain to be at least one fire-polishing length wide, but in practice, we want 10 or more fire-polishing lengths in the

domain for bubble merger to take place and the RT instability to become well developed. These restrictions limit us to consider densities $\leq 1.5 \times 10^7$ g cm^{-3} in the present study. The lower limit of densities we can consider is set only by what is attained in the supernova explosion itself—we stop at 6.67×10^6 g cm^{-3} here.

When the RT instability dominates the burning, it is the fluid motion mixing the fuel with the hot ash that controls the burning of the new fuel, rather than thermal conduction. Thus, the flame has a very large thermal width, governed by the mixing, at the lowest densities. To initiate a detonation, the temperature in a sufficiently large region needs to rise in unison, such that the over-pressure generated by the burning is strong enough to drive a shock just ahead of the burning layer. The critical size of this region is called the matchhead size. If this RT thermal width becomes as large as the critical detonation matchhead size, as tabulated in Niemeyer & Woosley (1997), it is possible that a DDT can occur. Furthermore, the size of the matchhead increases dramatically as the density decreases, and at low densities, it may be larger than the entire star. We note that recent simulations (Gamezo et al. 2003; Reinecke et al. 2002) indicate that a pure deflagration can be successful in unbinding the star. We will explore the possible of a DDT, using the scaling behavior we find for flames in the distributed burning regime.

3.   NUMERICAL METHODS

The simulations were performed using an adaptive, low Mach number hydrodynamics code, as described in Bell et al. (2003b). The state variables in the inviscid Navier-Stokes equations are expanded in powers of Mach number, following Majda & Sethian (1985). The result is that the pressure is decomposed into a dynamic and thermodynamic component, the ratio of which is of order Mach number squared. Only the dynamic component appears in the momentum equation. These equations are solved using an approximate projection formalism (Almgren et al. 1998; Day & Bell 2000), breaking the time evolution into an advection and a projection step. The advection is computed using an unsplit, second-order Godunov method that updates the species and enthalpy to the new time level and finds provisional velocities. A divergence constraint on the velocities is provided by the thermodynamics, and enforced in the projection step, where the provisional velocities are projected onto the space of vectors satisfying this constraint. Burning is handled through operator splitting. The low Mach number formulation allows us to follow the evolution of these slow moving flames—in this density range, the laminar speeds are M $\sim 10^{-5}$ (see Table 1)—without the constraint of the sound speed on the timestep. This affords us timesteps that are $O(1/M)$ larger than a fully compressible code would take. We are still free however to have large density jumps as

we cross the flame. This method was validated for astrophysical applications by comparing solutions of 1-d laminar flames to fully compressible results (Bell et al. 2003b), and in our study of the Landau-Darrieus instability (paper I), where the growth rate computed from our calculations matched the theoretical predictions across a range of wave numbers. The code is unchanged from the description in Bell et al. (2003b). We review the input physics used in the present simulations below.

This method contrasts sharply with that used in the only previous study of the RT instability in Type Ia SNe, as presented in Khokhlov (1995). There, the fully compressible PPM algorithm was used, along with a model for a thickened flame to represent it on the small scales. The laminar flame speed matched the correct physical value, but the flame thickness was much larger than the physical value. In the present case, resolving the thermal structure frees us from the need for a flame model.

The equation of state consists of a Helmholtz free-energy tabular component for the degenerate/relativistic electrons/positrons, an ideal gas component for the ions, and a black-body component for radiation, as described in Timmes & Swesty (2000). The conductivities contain contributions from electron-electron and electron-ion processes, and are described in Timmes (2000). All of the flames are half carbon/half oxygen, but only the carbon is burned. A single reaction, $^{12}C(^{12}C,\gamma)^{24}Mg$, is followed, using the unscreened rate from Caughlan & Fowler (1988). Since we do not expect the burning to proceed up to the iron-group elements at these low densities, this reaction alone is sufficient to model the nuclear reactions. The reaction rate for oxygen burning is several orders of magnitude slower than the carbon rate at the ash temperatures we reach, so neglecting oxygen burning is valid on our scales.

The calculations are initiated by mapping a one-dimensional steady state laminar flame (computed with the same code) onto our grid, shifting the zero point according to a random phase, 10 frequency sinusoidal perturbation. Beginning with a steady-state flame in pressure equilibrium virtually eliminates any transients from disturbing the flow ahead of the flame. In all of the results presented, the flame is moves toward decreasing y in our domain. The transverse boundaries are periodic, the upper boundary is outflow, and the lower boundary is inflow, with the inflow velocity set to the laminar flame speed. This keeps an unperturbed flame stationary on our grid. The solutions presented here were computed with an advective CFL number of 0.225 and typically required 8000 timesteps. For all the runs we present, adaptive mesh refinement was used, with a base grid plus one finer level that has twice the resolution. This allows us to focus the resolution on the interesting parts of the flow, allowing larger domains to be studied. Refinement triggered on the temperature gradient and the gradient of carbon mass fraction, ensuring that the flame's reaction zone was always at the finest resolution.

4. RESULTS

Table 2 lists the parameters used for all the simulations we present. For the lowest density case, 6.67×10^6 g cm^{-3}, we actually present results for three different domain sizes and two resolutions and for the 10^7 g cm^{-3} case, we present an additional simulation with the burning disabled. Except where noted otherwise, all discussion of the 6.67×10^6 g cm^{-3} results refer to the widest domain run. In the discussion below, we first concentrate on the change in character of the burning as the density is changed. Next we look at integral quantities that help characterize the flame, followed by a measurement of the RT growth rate and a comparison of the RT instability with and without burning. Finally, we consider resolution and domain size effects on the results we present.

4.1. Varying the Density and the Transition to Distributed Burning

Figures 1 to 3 show the results for the three densities we consider in this paper, 6.67×10^6 g cm^{-3}, 10^7 g cm^{-3}, and 1.5×10^7 g cm^{-3}. The fuel is at the bottom of the domain (and colored red), and the ash is at the top of the domain. Gravity points up, toward increasing y, in all simulations. For all runs, we set $g = 10^9$ cm s^{-2}. This value is appropriate for the outer regions of the star, and assumes that some pre-expansion of the white dwarf has taken place. The domain width was chosen based on the flame width and fire-polishing length (and considerations of how many zones we can reasonably compute) to contain several unstable wavelengths. We see from the figures that as the density increases, the small scale structure is greatly diminished, as the burning is more effective in containing it. The calculations were run until the instability reached the top or bottom of the computational domain, or the size of the mixed region grew to be much larger than the width of the domain, leading to saturation of the instability which will be discussed later. In the descriptions below, 'bubble' refers to the hot ash buoyantly rising into the cool fuel, and 'spike' refers to the cool fuel falling into the hot ash.

The results for $\rho = 6.67 \times 10^6$ g cm^{-3}, 768 cm wide simulation (Figure 1) shows the flow quickly becoming mixed and the initial perturbations rapidly merging together. A mixed region 500–1000 cm wide forms, separating the fuel and ash. Some smaller features begin to burn away as the flame evolves and the ash gets entrained by the fluid motions. At late times, it becomes impossible to draw a well defined flame surface separating the fuel and ash, as the RT mixing clearly dominates. In §4.4, we look at the effect of different domain widths on this growth.

The 10^7 g cm^{-3} run (Figure 2) shows a balance between the RT growth and the burning.

Spikes of fuel push well into the hot ash, forming well defined mushroom caps. Before these caps can travel too far into the ash, they burn away. This is seen for several spikes in Figure 2—the mushrooms gradually burn away, almost uniformly, turning yellow/green, and finally leaving a ephemeral outline in the ash as the burning completes. As the instability evolves, we see longer wavelength modes beginning to dominate, but they also begin to burn away. We are prevented from watching the final dominant mode that grows burn away because of it reaching the top of our domain.

The highest density case, 1.5×10^7 g cm^{-3} (Figure 3) behaves qualitatively different than the two lower densities. A defining characteristic of this density is that the flame front is always sharply defined—a trait that we expect to carry over to higher densities as well. At this density, the burning proceeds rapidly enough that it can suppress the RT instability significantly. This is as expected, since the fire-polishing length is larger than the flame width at this density (see Table 1). As the spikes of fuel extend into the hot ash, we see them rapidly burning away from the outside inward. The RT mushroom caps hardly have time to form before their ends are burned away, giving them a hammerhead-like appearance.

Figure 4 shows the carbon destruction rate, $|\dot{\omega}_C|$, at the midpoint of each calculation for the three densities. The figures are shown at nearly the same scale in terms of flame widths, at 137, 86.2 and 99.1 l_f wide for the 6.67×10^6 g cm^{-3}, 10^7 g cm^{-3}, and 1.5×10^7 g cm^{-3} simulations respectively. At the low density end, the burning is concentrated in small regions whereas at the high end, the burning is smoother. We would expect this trend to continue for densities outside the range we consider here. At higher densities, the burning will dominate even more, and we would expect the flame surface to be well defined on the small scales. At densities lower than 6.67×10^6 g cm^{-3}, the mixed region will grow even larger, as the burning becomes even less effective at suppressing the RT instability. We will look at how the width of the reactive region grows in proportion to that of the mixed region at these low densities in §4.3.

4.2. Wrinkling and Acceleration of the Flame

Having described the overall evolution of the flames, we now present some quantitative measures of flame behavior. We define the effective flame speed, V_{eff}, in terms of the carbon consumption in the domain; namely,

$$V_{\text{eff}}(t) = -\frac{\int_\Omega \rho \dot{\omega}_C d\mathbf{x}}{W(\rho X_C)^{\text{in}}} \tag{6}$$

where Ω is the spatial domain of the burning region, W is the width of inflow face, $(\rho X_C)^{\text{in}}$ is the inflow carbon mass fraction, and $\rho \dot{\omega}_C$ is the rate of consumption of carbon due to nuclear

burning. Accurate direct evaluation of this integral is problematic because of the operator split treatment of reactions in the numerical method. A robust and accurate estimate of V_{eff} can be obtain by integrating the conservation equation for carbon mass fraction $\partial(\rho X_C)/\partial t + \nabla \cdot (\rho u X_C) = -\rho \dot{\omega}_C$ over Ω and a time interval $[T_1, T_2]$ to obtain

$$V_{\text{eff}} = \frac{\int_\Omega (\rho X_C)|_{T_1}^{T_2} d\mathbf{x}}{(T_2 - T_1)W(\rho X_C)^{\text{in}}} - u^{\text{in}} \tag{7}$$

u^{in} is the inflow velocity. Note that this formula is only valid when essentially all carbon is being consumed in the domain.

Another quantity of interest is the area of the flame, which for our two-dimensional studies is a length. Computing a flame length for the lower density cases is problematic since there is often not a distinct flame surface. In this paper we define a flame length as the number of zone edges where the carbon mass fraction passes through 0.25. We normalize the length to the initial flame length so we can measure the growth of the burning surface. This approach, while crude, is robust and defines a reasonable method for computing the length of a well mixed flame where other approaches are infeasible. In particular, this approach systematically overestimates the flame length; however, this can be compensated for by normalizing by the initial flame length. We have validated that for well-defined flames, this method agrees well with the length of a contour as computed with the commercial IDL package, after normalization. Furthermore, when the flame is well-defined, the length is relatively insensitive to the choice of the mass fraction threshold, varying by at most 10% as the threshold is varied between 0.125 and 0.375.

Figures 5 to 10 show the speeds and lengths of the flames at the three densities as a function of time (the additional curves on the 6.67×10^6 g cm^{-3} plots will be discussed in §4.4). The maximum speedups we observe are 3 times the laminar speed for the 6.67×10^6 g cm^{-3} run, 5 times for the 10^7 g cm^{-3} run, and 2.5 times for the 1.5×10^7 g cm^{-3} run. These speedups are much larger than any seen in our companion study on the Landau-Darrieus instability (paper I), as expected, based on the outcome of the large scale simulations of the explosion. The flame length increases by a factor of 50 throughout the simulation for the two lowest densities, but only increases to by a factor of 8 for the 1.5×10^7 g cm^{-3} case, due to the strong moderation of the RT instability by the burning.

Comparing the velocity curves to the length curves, we see that, in general, the velocity is not strictly proportional to the flame surface area. This is not unexpected, since the stretch and curvature that the flame experiences as well as the complicated motions of the RT instability pushing the fuel and ash together will modify the local burning rate. Evidence of this variability is seen in Figure 4 where considerable variation in the carbon destruction rate is observed, even for the highest density case. To further quantify this effect, in Figures 11

to 13 we plot the velocity divided by flame surface area normalized to v_{laminar}/W, where W is the width of the box. With the caveat that there are ambiguities in defining flame surface area for the "distributed" flames, we observe that, after an initial transient, the flame speed versus area relaxes to an essentially statistically stationary value. For the highest density case, the effective flame velocity is approximately 30% of the laminar flame speed × the area enhancement. For the lower density cases, the value drops to approximately 10%. Thus, at these densities, we find

$$v(t) = \beta \ v_{\mathrm{laminar}} \frac{A(t)}{A_0} \ , \tag{8}$$

where β is a proportionality constant not equal to 1. This proportionality constant increases with density, reflecting the fact that the fire-polishing wavelength, which sets the smallest scale on which we can wrinkle the flame, grows as well. Thus at higher densities, the localized curvature is smaller, and as a result, the localized velocity is less affected.

This deviation from purely geometric scaling has strong implications for subgrid models, particularly in the flamelet regime, where it is normally assumed that the velocity scales directly as the increase in area of the flame surface. It appears that this is not the case, and is further complicated by the density dependence of the proportionality constant. Comparisons can be made with other flame calculations. Röpke et al. (2003), using a level-set approach, with a fixed flame speed to model the pure Landau-Darrieus instability, find an enhancement of the velocity over the corresponding area increase, although, β is still close to unity. Our deviation is both larger in magnitude, and opposite in sense, likely due to the implicit inclusion of curvature effects on the flame. Our present results agree with the trend observed in our Landau-Darrieus study (paper I).

Woosley (1990) introduced a fractal model to describe the growth of the flame surface in a supernova when the burning is in the flamelet regime. The self-similar range through which a fractal description applies is bounded by the fire-polishing length on the small scales and the Sharp-Wheeler description for the RT instability growth on the large scales. In two-dimensions, a fractal model for the growth of the flame surface would be

$$L = L_0 \left(\frac{\lambda_{\max}}{\lambda_{\min}} \right)^{D-1} = L_0 \left(\frac{\alpha g_{\mathrm{eff}}^2 (t - t_0)^2}{4\pi v_{\mathrm{laminar}}^2} \right)^{D-1} \ , \tag{9}$$

where we expect $1 < D < 2$ in the self-similar scaling regime. The offset in time, t_0, is chosen such that $L = L_0$ at $t = 0$. The value of α is taken to be 0.05. As we will see in §4.3, the Sharp-Wheeler model may not be the proper description of the reactive RT instability. With that caveat, Figures 8 and 10, we plot the predictions of the fractal scaling model using $D = 1.5$ and 1.7, which give area growing as t and $t^{1.4}$ respectively. From these figures, it seems that, if this fractal model is correct, the growth in the flame surface

is closely represented by a fractal dimension of 1.7. This agrees with the value computed from two-dimensional RT studies by Hasegawa et al. (1996). Some evidence suggests that the fractal dimension of RT induced turbulence may increase with time (Dimotakis et al. 1998). We caution however that we only span about a decade between $\lambda_{\min}$ and $\lambda_{\max}$ in these simulations. If such a scaling holds, it could serve as a subgrid model for large scale simulations, however, the evolution of the proportionality constant in Equation (8) needs to be understood. Additional calculations that encompass a larger range of spatial scales are needed to further validate this model.

Not all of the energy release by the flame goes into driving the expansion of the star. The RT unstable flame and associated Kelvin-Helmholtz instabilities also generate turbulence. Turbulence diagnostics can be difficult to define—here we use an integral quantity, the Favre average turbulent kinetic energy which plays a role in the $k - \epsilon$ subgrid model for turbulence. The Favre average turbulent kinetic energy (for a discussion of which see Peters 2000), can be written

$$\tilde{k}(y,t) = \frac{1}{2} \left\langle (\rho\mathbf{v} - \langle\rho\mathbf{v}\rangle)^2 \right\rangle / \langle\rho\rangle^2 \tag{10}$$

where $\langle\cdot\rangle$ denotes the horizontal spatial average of the quantity enclosed in the brackets. Figure 14 shows $\tilde{k}$ as a function of height at several instances in time for the 6.67×10^6 g cm^{-3} flame. We see that, within the mixed region, the turbulent kinetic energy is roughly constant, and this plateau rises quadratically with time, as shown in Figure 15. The integral of $\tilde{k}(y,t)$ over the vertical extent of the domain is the total turbulent kinetic energy $k(t)$. The generation of turbulent kinetic energy as a function of time is shown for the three densities in Figures 16 to 18. The data suggest that the increase in kinetic energy as a function of time is well approximated by a power law of the form

$$k(t) = at^b \ , \tag{11}$$

are shown in Figures 16 to 18, and summarized in Table 3. The power law fits, summarized in Table 3 match the data quite well, giving an exponent, $b = 2.3$–2.8, depending on the density, with the power increasing with increasing density. In the lowest density run, there is considerable turbulent energy, and, as Figure 14 shows, $\sim 10^{11}$ erg g^{-1} is reached after 6.4×10^{-3} s. This is on a scale of $\sim 10^3$ cm. Niemeyer & Hillebrandt (1995b) presumed pre-existing turbulent kinetic energy of this level on scales of 10^6 cm in their main calculation. Assuming a one-third power scaling of the energy cascade, on their length scales the RT generate turbulence already overwhelms this pre-existing turbulence, and it is continuing to grow, apparently quadratically with time. These results suggest that the RT instability alone can provide the turbulent motions presumed to exist in the star.

4.3.   The Growth Rate of RT Unstable Flames

In the absence of any reactions, the extent of the mixed region should increase as t^2, as predicted by the Sharp-Wheeler model, Equation (1). This relation is only expected to hold during the phase where bubbles are merging, which excludes the initial linear growth range. Also, because we are resolving the flame structure, the interface between the fuel and ash is not infinitesimally thin, which complicates the definition of the Atwood number. Furthermore, at late times, once the bubble merging in our domain has stopped and the size of the mixed region rivals the width of the domain, this relation will also break down. This relation was derived for the purely hydrodynamical RT instability. Burning can have large consequences here. The Sharp-Wheeler model describes the growth of this mixed region, which will contain fuel and ash, but that fuel is burning, and as it turns into ash, we would expect to find the mixed region smaller than that of the purely hydrodynamical case. For the present simulations, since we have a limited number of modes in our box (typically 10), we are only going to be able to do the fits on a small subset of the data. A future study will focus on scaling in the flamelet regime, using much larger domains.

Figures 19 to 21 show the extrema of the mixed region, computed by laterally averaging the carbon mass fractions and finding the positions where it first exceeds 0.05 and 0.45. This definition is consistent with that used in Khokhlov (1995). The curves are measured with respect to the initial position of the interface. The top curve measures the position the spikes of fuel pushing into the region of hot ash. The lower curve is the position of the bubbles of hot ash floating into the fuel. The sharp kinks in the spike curves represent the instances where the plume of fuel, having pushed far into the ash region, burned away. At the highest density (Figure 21), the bubble curve is very smooth.

We can make fits of the growth of the mixed region to time by fitting to a power law,

$$w(t) = ct^n \ . \tag{12}$$

We do not attempt to fit to the Sharp-Wheeler scaling and find a value of α because of the limited range of wavelengths we follow, and the uncertainty as to whether that relation holds in the reactive case. We exclude the initial linear phase of the growth of the RT instability in our fits. Figures 22 to 24 shows the results. In all cases, we find n less than 2.0, indicating that we are not in the Sharp-Wheeler regime. Furthermore, n increases with increasing density. We find $n = 1.16$ for 6.67×10^6 g cm^{-3}, $n = 1.2$ for 10^7 g cm^{-3}, and $n = 1.55$ for 1.5×10^7 g cm^{-3}. Larger scale studies, with a greater range of wavelengths are needed to determine whether this is a general result for reactive Rayleigh-Taylor, or if this is because of the small size domains considered here. One way we can get some insight into this is to rerun one of these simulations without burning. (Note that in this case, we shift to a non-moving

frame of reference whereas the reacting cases are performed in a reference frame moving at the laminar flame speed.) The growth rate for the 10^7 g cm^{-3} run with burning disabled is over-plotted in Figure 20. We see that it is much smoother than the corresponding reactive case, since the spikes of fuel which push into the hot ash never burn away. The only wiggles in the mixing region growth curves result from bubble mergers. The fit to a power law for this non-reactive simulation is presented in Figure 25. The carbon mass fraction for several points in time are shown in Figure 27, which compares directly to Figure 2. Here, $n = 1.36$, higher than the reactive case, but still not equal to 2.0. The difference between this value and the reactive case shows that the burning does have some influence. In the non-reactive case we really do expect $n = 2.0$, and therefore the difference we see is very likely because we also are probably not following enough modes to see the Sharp-Wheeler scaling.

For the 1.5×10^7 g cm^{-3} run, we were closest to growing as t^2. The burning here is quite vigorous, compared to the RT growth, so as argued above, we would expect to see its influence on the extent of the mixed region. However, we would expect it to affect the position of the spikes of fuel only, since the bubbles of ash do not react. Therefore, we can fit the growth of the bubbles and spikes from the initial interface separately. This is shown in Figure 26. Again, we exclude the initial linear growth phase of the instability. We find the bubble position growing as $n = 1.85$ and the spike region growing as $n = 1.28$. Based on the trends we see here and above, we would expect that once we have enough unstable modes in the box, the width of the mixed region during the bubble merger phase will scale as slightly smaller t^2, with the bubble position itself growing as t^2. Therefore, more studies, in larger domains with more unstable modes are needed.

It is interesting to look at how the size of the reactive region scales with that of the mixed region, especially at the lowest density. As discussed in §2, if the reactive region grows to the size of the detonation matchhead, then it may be possible for a deflagration-detonation transition to occur. Measuring the scaling of the reactive region to the mixed region is not easy, because the flame is so wrinkled. We will use a volume weighted definition here. The collection of zones, A, where the carbon mass fraction, X_C, is between $\eta_{\min}$ and $\eta_{\max}$ is

$$A \equiv \left\{ X_{C\,(i,j)} \;\middle|\; \eta_{\min} \leq X_{C\,(i,j)} \leq \eta_{\max} \right\} \; . \tag{13}$$

Similarly, we can define the collection of zones, B, where the density-weighted carbon destruction rate, is within γ of the peak,

$$B \equiv \left\{ \left(\rho \dot{X}_C\right)_{(i,j)} \;\middle|\; \left(\rho \dot{X}_C\right)_{(i,j)} \leq \gamma \max\left(\left(\rho \dot{X}_C\right)_{(i,j)} \right) \right\} \; . \tag{14}$$

Then, the ratio of the size of the reactive region to the mixed region is

$$\Gamma = \frac{V_B}{V_A} \; , \tag{15}$$

where V_A is the volume of the zones in set A. Once the mixed region develops, we expect this quantity to be always less than unity. Because of the freedom to choose the parameters $\eta_{\min}$, $\eta_{\max}$, and γ, the numerical value of Γ itself does not have much meaning, but the trend with time does. We pick $\eta_{\min} = 0.05$, $\eta_{\max} = 0.45$, and two values of γ: 0.1 and 0.8. We note that the trend is relatively insensitive to the choice of these parameters, as illustrated by Figure 28, which shows Γ as a function of time for the 6.67×10^6 g cm^{-3} RT unstable flame for the two choices of γ. After an initial transient, it appears that these curves level off, indicating that the reactive region continues to growth in size proportional to the mixed region as the flame evolves. We note that this shows that the reactive region is a small fraction of the mixed region, but this absolute scaling is dependent on the choice of the three parameters. This is illustrated in Figure 29, where the mixed and reactive regions are shown, midway through the calculation. At late times, the peak nuclear energy generation comes from regions where the carbon mass fraction is ~ 0.15, as shown in Figure 30. This is also apparent by looking at the laterally averaged flame profile and comparing to the laminar state—see Figure 31. If this reactive region can growth to a critical matchhead size, before the entire star is consumed, it may be possible for a deflagration to detonation transition to proceed. However, since at late times the peak burning is occurring at mass fractions of 0.15 rather than 0.5, this will greatly increase the required matchhead size, further complicating the possibility of a deflagration-detonation transition.

4.4. Resolution and Domain Size Dependence on the Results

In this subsection, we examine the role of domain size and resolution on the computational results. Figures 32 and 33 show the evolution of the 6.67×10^6 g cm^{-3} RT simulation in narrower domains (96 cm and 384 cm wide respectively). Other than the domain size, the parameters are identical to those used in the results described shown in Figure 1. In the narrowest case, once the size of the mixed region reaches a fixed size, comparable to the width of the domain, the mixing and reacting processes saturate and the flow enters a quasi-steady-state, with vortices that are remnants of the early mixing driving transverse shear flow in the mixed region. Once this saturation is reached, the burning rate begins to slowly decay. This behavior is not seen in the corresponding wider domain calculation, although, we would expect a similar pattern if we use a taller domain and ran out to longer times.

Figure 5 shows three additional curves corresponding to these narrower domains, the narrowest at two different resolutions (see Table 2). In the 96 cm wide domain, the peak velocity is much smaller, reaching only about 3 times the laminar speed. This is to be expected

from Equation (2)—the wider domain allows longer wavelength modes to go unstable. The decrease in velocity at late times in the narrow domain begins when the size of the mixed layer becomes comparable to the width of the domain, preventing any further modes from growing. This is reflected in the later panels of Figure 32. In the 384 cm wide domain, the velocity continues to grow, beyond 6 times the laminar speed—we would expect our widest domain run to continue to accelerate as well, but it began to interact with the top of our computational domain and was not run out as long.

The velocity of the low resolution run tracks that of the high resolution case very closely, suggesting that, for the large scale diagnostics, we have converged. This lowest resolution run has approximately 5 points in the thermal width (Equation 5), a value found acceptable in the convergence study performed in Bell et al. (2003b) for Landau-Darrieus unstable astrophysical flames. We note again that this definition of thermal width is smaller than some other commonly used definitions (see, for example Dursi et al. 2003). Finally, in all calculations, the initial perturbations are well resolved, with typically 50–100 zones per wavelength (with the only exception being the 96 cm wide, 6.67×10^6 g cm^{-3} run, where there are only 20 zones per wavelength). This zoning is at or exceeds the resolution determined to give acceptable convergence of single-mode RT growth rates in the 3-d compressible study presented in Calder et al. (2002).

We also can look at how the scaling of the turbulent kinetic energy depends on the domain size. For the 384 cm wide, 6.67×10^6 g cm^{-3} run, this is shown in Figure 34. Two fits are shown. When all of the data is included, the fit is quite poor, since it is biased by by data at the end of the run when the mixing has saturated and the turbulent kinetic energy stops increasing. Excluding this data, the fit to the first 0.005 s is quite good, and with the kinetic energy $\sim t^{2.325}$ quite close to the 2.267 power obtained from the 768 cm wide run. Thus, it appears that the scaling of the turbulent kinetic energy prior to saturation is insensitive to the domain size.

5.   DETONATION IN THE DISTRIBUTED REGIME?

Based upon the observed systematics of flame propagation in the distributed regime, we can begin to speculate on the potential for a transition to detonation. As discussed by Niemeyer & Woosley (1997) and Niemeyer (1999), there are two possible modes for a delayed transition to detonation: a) a "local" transition to detonation because a fluid element of critical mass burns with a supersonic phase velocity and b) a "macroscopic" transition because some appreciable fraction of the white dwarf volume develops such complex topology that burning briefly consumes more fuel than could a spherical front encompassing that region

and moving at supersonic speed. The former, also known as the Zeldovich mechanism, is the basis for the "delayed detonation model" by Khokhlov (1991); the latter is the basis for a similar model by Woosley & Weaver (1994). Niemeyer (1999) has argued that the volume detonation model requires special preconditioning, but because we study only the small scales on which the flame is resolved, we cannot comment in a meaningful way on this issue. Also, because we have not included turbulence cascading down from scales larger than our grid, we cannot conclusively argue about the local transition to detonation either (a large amount of turbulence could, for example, induce a transition to distributed burning at a higher density). Still some scaling relations are observed that, if they can be generalized by larger scale studies, argue against a transition to detonation.

As is well recognized (e.g. Niemeyer 1999), transition to detonation can never occur so long as a well defined flame exists. The width of a steady flame is always thinner than the critical mass required for detonation. However, a mixture of hot fuel and cold ash is potentially explosive as calculations in the SN Ia context (Lisewski et al. 2000) have suggested. Figure 4 shows the existence, in the distributed regime, of localized hot spots of unsteady burning. The high temperature sensitivity of the $^{12}C + {}^{12}C$ reaction itself makes it difficult for one of these hot spots to become supercritical in mass. For the conditions we consider, carbon fusion dominates the energetics, and the energy production is

$$S_{\mathrm{nuc}} \; \propto \; X_C^2 \, T^n \; , \tag{16}$$

where X_C is the mass fraction of carbon, and n given by the Coulomb barrier between two carbons nuclei,

$$n \; = \; \frac{\tau - 2}{3} \; , \tag{17}$$

$$\tau \; = \; 4.248 \left(\frac{Z_1^2 \, Z_2^2 \, \bar{A}}{T_9} \right)^{1/3} \tag{18}$$

$$= \; 84.13 \, T_9^{1/3}, \tag{19}$$

with T_9 the temperature in 10^9 K. For our calculations with $\rho = 6.67 \times 10^6$ g cm^{-3}, the temperature of the hot ash is $T_9 = 2.4$. Anticipating that the temperature of a combustible fuel-ash mixture will not be far from that, we find $n \approx 20$. The carbon mass fraction in the fuel is 0.5 and in the ash it is zero, and the temperature of the unburned fuel is negligible.

In any mixed mass, M, composed of fractions f of ash and $1 - f$ of fuel, the temperature will be

$$T_{\mathrm{mix}} \; = \; f \, \frac{C_{\mathrm{P}}(T_{\mathrm{ash}})}{C_{\mathrm{P}}(T_{\mathrm{mix}})} \, T_{\mathrm{ash}} \tag{20}$$

and the carbon mass fraction

$$X_{C,\text{mix}} \approx (1-f) X_{C,\text{fuel}} . \tag{21}$$

The dependence of the heat capacity on temperature is important and mitigates somewhat the extreme sensitivity of the reaction rate. In the vicinity of $T_9 = 2.5$, the heat capacity is predominantly due to the electron gas (with $C_{P,e} \propto T$), but with a non-negligible contribution from radiation ($C_P \propto T^3$) (Woosley et al. 2003). To good approximation, near $T_9 = 2.5$, $C_P \propto T^{7/4}$.

The maximum in energy generation will then occur for

$$\frac{d}{df}[(1-f)^2 \, f^{80/11}] = 0 , \tag{22}$$

or for $f \approx 40/51 = 0.784$—that is, in the burning mixture, $X_C = 0.11$ and $T_9 = 2.20$. A factor of two variation in the energy generation occurs for $0.60 < f < 0.91$, or X_C from 0.045 to 0.20. This agrees well with what is observed in the numerical simulation (Fig. 30).

Coupled with the fact that burning to magnesium or silicon releases less energy than burning to the iron group, this low carbon mass fraction implies that the overpressure from burning will be small in the regions where ash and fuel are mixed. Burning from $T_9 = 2.2$ to 2.4, the typical ash temperature, will only raise the pressure by 8%. Since this overpressure determines the temperature reached in a detonation and the burning rate depends on this to a high power, the critical mass for initiating a detonation will be large. The size will certainly be greater than the distance a sound wave can travel during the time it takes the mixture to burn. At $T_9 = 2.2$ and $X_C = 0.11$, the nuclear time scale is

$$\tau_T \approx \frac{C_P}{\dot{S}_{\text{nuc}}} , \tag{23}$$

or about 0.07 s. The speed of sound is approximately 5000 km s^{-1}. Hence a critical mass for these conditions must be at least 300 km in size.

On the other hand, Figure 28 shows that, in steady state, the size of the reactive region is approximately a small constant times the size of the mixed region. Even allowing a range of burning time scales of a factor of 10 across the burning region, the explosive mixture only has dimensions about 10% that of the region that has been mixed by the RT instability. Taking $0.05g_{\text{eff}}t^2$ as an upper bound to that (see §4.3), and realizing that the temperature will decline still further in a few tenths of a second because of expansion, the largest mixed, potentially explosive region is less than 5 km. Thus, though a localized transition to detonation is in principal possible, there simply may not be room, nor time enough to develop one in an exploding white dwarf.

6. CONCLUSIONS

We presented direct numerical simulations of reactive RT instabilities in conditions appropriate to the late stages of a Type Ia supernova explosion. Fully resolving the flame frees us from the need to specify any model parameters, such as the flame speed, Markstein length, etc. In the density range we consider, the flame transitions from having a distinct, well defined interface at the high density end to being a chaotic, well mixed burning region at the lower density end, with a transition density of $\sim 10^7$ g cm^{-3}. This transition is expected based on the arguments presented in §2. Furthermore, this would suggest that at the even higher densities characteristic of the early stage of the explosion, the flame surface continues to be well defined, consistent with the conclusions of Niemeyer et al. (1999) and the 2-d flame-model simulations at 10^8 g cm^{-3} presented in Khokhlov (1994). The effects of the burning were further made concrete by presenting the 10^7 g cm^{-3} case both with and without reactions.

At the lowest density, the mixed region becomes very large, although, still smaller than the critical carbon detonation matchhead size (Niemeyer & Woosley 1997). It appears that the reactive region grows in direct proportion to the size of the mixed region, making it possible in theory that such a transition can occur, however, at these low densities, much of the star is already consumed, and, based on scaling predictions from the present simulations, the time required for the reactive region to grow to the matchhead size seems to be longer than the total explosion time. In effect, the flame runs out of star before a critical mass can be built up. Future simulations will explore this in more depth.

In all cases presented here, the flames accelerated considerably, reaching speeds between 2 and 6 times the laminar flame speed. This is significantly larger than accelerations seen in small-scale/resolved Landau-Darrieus instability studies (paper I). The growth of the flame surface appeared to be well described by a fractal model, with a fractal dimension of ~ 1.7. In the cases considered, the effective flame speed was asymptotically proportional to the increase in flame surface area but the constant of proportionality was about 0.1 for the low density cases and 0.3 for the higher density case. Thus, the flame acceleration was considerably less than would be predicted by the increase in flame surface area alone. This proportionality constant may approach unity as the density is increased, because the smallest scale on which the RT instability can bend the flame (the fire-polishing length) increases dramatically with density, and therefore the magnitude of the curvature that the flame experiences locally decreases. We would expect that on larger domains the flame would continue to accelerate, further supporting the already widely held view that the RT instability provides most of the acceleration to the flame in a pure deflagration Type Ia SNe explosion.

The growth of the mixed region for the reactive RT instability appears to be slower than the non-reactive case. The present results do not seem to support the Sharp-Wheeler model, but larger scale studies are needed, with more bubbles merging over a longer period of time to better understand the growth of the mixed region. Understanding the growth of the mixed region is critical to providing an accurate subgrid model.

Future studies will focus on the three-dimensional counterparts to the flames we discussed here. Turbulence behaves very differently in two and three dimensions, so we expect to see some differences in the evolution of the instability. Numerical results indicate that the growth rate of the pure RT instability is faster in 3-d than in 2-d (Kane et al. 2000; Calder et al. 2002). Furthermore, in 3-d the surface to volume ratio of the spikes of fuel is larger than in 2-d, exposing more fuel to the hot ash, so we may expect them to burn away more quickly. We still expect, based on the arguments presented in §2 and the results of the simulations, that the flame will undergoing the same transition in behavior as the density decreases. Larger two-dimensional studies in the flamelet regime are also needed, moving toward higher densities. Capturing a greater range of scales on the grid will allow for validation of the fractal scaling model and a better understanding of the moderation of the Sharp-Wheeler prediction for the growth of the mixed region. Finally, these fully resolved simulations can serve as the basis for testing various models to represent the flame on subgrid scales, which become necessary to address the larger scale Type Ia physics.

REFERENCES

Almgren, A. S., Bell, J. B., Colella, P., Howell, L. H., & Welcome, M. 1998, J. Comput. Phys., 142, 1

Arnett, W. D., Truran, J. W., & Woosley, S. E. 1971, ApJ, 165, 87

Bell, J. B., Day, M. S., Rendleman, C. A., Woosley, S. E., & Zingale, M. A. 2003a, Astrophysical Journal, accepted, paper I

—. 2003b, Journal of Computational Physics, accepted

Calder, A. C., Fryxell, B., Plewa, T., Rosner, R., Dursi, L. J., Weirs, V. G., Dupont, T., Robey, H. F., Kane, J. O., Remington, B. A., Drake, R. P., Dimonte, G., Zingale, M., Timmes, F. X., Olson, K., Ricker, P., MacNeice, P., & Tufo, H. M. 2002, ApJS, 143, 201

Caughlan, G. R., & Fowler, W. A. 1988, Atomic Data and Nuclear Data Tables, 40, 283, see also http://www.phy.ornl.gov/astrophysics/data/cf88/index.html

Chandrasekhar, S. 1981, Hydrodynamic and Hydromagnetic Stability (New York: Dover)

Colella, P., & Woodward, P. R. 1984, J. Comp. Phys., 54, 174

Cook, A. W., & Dimotakis, P. E. 2001, J. Fluid Mech., 443, 69

Darrieus, G. 1938, in La Technique Moderne, France

Davies, R. M., & Taylor, G. 1950, Proc. R. Soc. London A, 200, 375

Day, M. S., & Bell, J. B. 2000, Combust. Theory Modelling, 4, 535

Dimotakis, P. E., Catrakis, H. J., Cook, A. W., & Patton, J. M. 1998, Presented at the 2nd Monte Verita Colloquium on Fundamental Problematic Issues in Turbulence, 22-28 March 1998 (Ascona, Switzerland). GALCIT Report FM98-2

Dursi, L. J., Zingale, M., Calder, A. C., Fryxell, B., Timmes, F. X., Vladimirova, N., Rosner, R., Caceres, A., Lamb, D. Q., Olson, K., Ricker, P. M., Riley, K., Siegel, A., & Truran, J. W. 2003, ApJ, 595, 955

Gamezo, V. N., Khokhlov, A. M., Oran, E. S., Chtchelkanova, A. Y., & Rosenberg, R. O. 2003, Science, 299, 77

George, E., Glimm, J., Li, X.-L., & Xu, Z.-L. 2002, PNAS, 99, 2587

Glimm, J., & Li, X. L. 1988, Phys. Fluids, 31, 2077

Hasegawa, S., Nishihara, K., & Sakagami, H. 1996, Fractals, 4, 241

Hillebrandt, W., & Niemeyer, J. C. 2000, Annu. Rev. Astron. Astrophys, 38, 191

Hoeflich, P., & Khokhlov, A. 1996, ApJ, 457, 500

Kane, J., Arnett, D., Remington, B. A., Glendinning, S. G., Bazán, G., Müller, E., Fryxell, B. A., & Teyssier, R. 2000, ApJ, 528, 989

Khokhlov, A. 1993, ApJ, 419, L77+

—. 1994, ApJ, 424, L115

Khokhlov, A. M. 1991, A&A, 245, 114

—. 1995, ApJ, 449, 695

Khokhlov, A. M., Oran, E. S., & Wheeler, J. C. 1997, ApJ, 478, 678

Kolmogoroff, A., Petrovsky, I., & Piscounoff, N. 1937, Bulletin de l'université d'état à Moscou (Série internationale), section A, 1, 1, reprinted and translated in P. Pelcé, Dynamics of Curved Fronts, Academic Press, Berkeley, CA, 1988

Landau, L. D. 1944, Acta Physicochimica, USSR, 19, 77, reprinted in P. Pelcé, Dynamics of Curved Fronts, Academic Press, Berkeley, CA, 1988

Layzer, D. 1955, ApJ, 122, 1

Lisewski, A. M., Hillebrandt, W., Woosley, S. E., Niemeyer, J. C., & Kerstein, A. R. 2000, ApJ, 537, 405

Livne, E. 1993, ApJ, 406, L17

Majda, A., & Sethian, J. A. 1985, Combust. Sci. Technol., 42, 185

Müller, E., & Arnett, W. D. 1982, ApJ, 261, L109

—. 1986, ApJ, 307, 619

Niemeyer, J. C. 1999, ApJ, 523, L57

Niemeyer, J. C., Busche, W. K., & Ruetsch, G. R. 1999, ApJ, 524, 290

Niemeyer, J. C., & Hillebrandt, W. 1995a, ApJ, 452, 779

—. 1995b, ApJ, 452, 769

Niemeyer, J. C., & Kerstein, A. R. 1997, New Astronomy, 2, 239

Niemeyer, J. C., & Woosley, S. E. 1997, ApJ, 475, 740

Nomoto, K., Thielemann, F.-K., & Yokoi, K. 1984, ApJ, 286, 644

O'Rourke, P. J., & Bracco, F. V. 1979, J. Comput. Phys., 33, 185

Peters, N. 2000, Turbulent combustion (Cambridge University Press)

Röpke, F. K., Niemeyer, J. C., & Hillebrandt, W. 2003, ApJ, 588, 952

Reinecke, M., Hillebrandt, W., & Niemeyer, J. C. 1999a, A&A, 347, 739

—. 2002, A&A, 391, 1167

Reinecke, M., Hillebrandt, W., Niemeyer, J. C., Klein, R., & Gröbl, A. 1999b, A&A, 347, 724

Sharp, D. H. 1984, Physica, 12D, 3

Taylor, G. 1950, Proc. R. Soc. London A, 201, 192

Timmes, F. X. 2000, ApJ, 528, 913

Timmes, F. X., & Swesty, F. D. 2000, ApJS, 126, 501

Timmes, F. X., & Woosley, S. E. 1992, ApJ, 396, 649

Vladimirova, N., & Rosner, R. 2003, Phys. Rev. E, 67, 066305

Woosley, S. E. 1990, in Supernova, ed. A. G. Petschek (New York: Springer-Verlag), 182

Woosley, S. E., Axelrod, T. S., & Weaver, T. A. 1984, in ASSL Vol. 109: Stellar Nucleosynthesis, 263

Woosley, S. E., & Weaver, T. A. 1994, in Supernovae, Les Houches, Session LIV, ed. S. A. Blundman, R. Mochkovitch, & J. Zinn-Justin (Amsterdam: North-Holland), 63–154

Woosley, S. E., Wunsch, S., & Kuhlen, M. 2003, ApJ, submitted, astro-ph/0307565

Young, Y.-N., Tufo, H. M., Dubey, A., & Rosner, R. 2001, J. Fluid Mech., 447, 377

Zingale, M., Niemeyer, J. C., Timmes, F. X., Duris, L. J., Calder, A. C., Fryxell, B., Lamb, D. Q., MacNeice, P., Olson, K., Ricker, P., Rosner, R., Truran, J. W., & Tufo, H. M. 2001, in Relativistic Astrophysics: 20th Texas Symposium, 490

Table 1: Properties of 0.5 ^{12}C/0.5 ^{16}O flames. colorred is the ρ in $\Delta\rho/\rho$ actually $\bar{\rho}$

ρ (g cm^{-3})	$\Delta\rho/\rho$	v_{laminar} (cm s^{-1})	l_f[a] (cm)	λ_{fp}[b] (cm)	M
6.67×10^6	0.529	1.04×10^3	5.6	0.026	3.25×10^{-6}
10^7	0.482	2.97×10^3	1.9	0.23	8.49×10^{-6}
1.5×10^7	0.436	7.84×10^3	0.54	1.8	2.06×10^{-5}

[a]Equation 5.
[b]Equation 4, taking $g = 10^9$ cm s^{-2}.

Table 2: Parameters for the RT simulations.

ρ (g cm^{-3})	width (cm)	height (cm)	Δx_{fine}[a] (cm)	width/l_f	width/l_{fp}	$l_f/\Delta x_{\text{fine}}$	comments
6.67×10^6	96.0	3072.0	1.0	17.1	3290	5.6	$\cdots$
	96.0	1536.0	0.5	17.1	3290	11.2	$\cdots$
	384.0	2304.0	1.0	68.6	14800	5.6	$\cdots$
	768.0	2304.0	1.0	137	29500	5.6	$\cdots$
10^7	163.84	327.7	0.16	86.2	712	11.9	$\cdots$
	163.84	327.7	0.16	86.2	712	11.9	no burning
1.5×10^7	53.5	107.0	0.0522	99.1	29.7	10.3	$\cdots$

[a]Δx_{fine} is the zone width on the finest mesh. In all simulations, $\Delta x = \Delta y$.

Table 3: Turbulent kinetic energy fits to $k(t) = at^b$.

ρ (g cm^{-3})	a	b	comments
6.67×10^6	1.169×10^{17}	1.626	384 cm wide; all data
	8.602×10^{18}	2.325	384 cm wide; initial 0.005 s
	6.514×10^{18}	2.267	768 cm wide
10^7	8.597×10^{18}	2.591	$\cdots$
1.5×10^7	2.202×10^{19}	2.867	$\cdots$
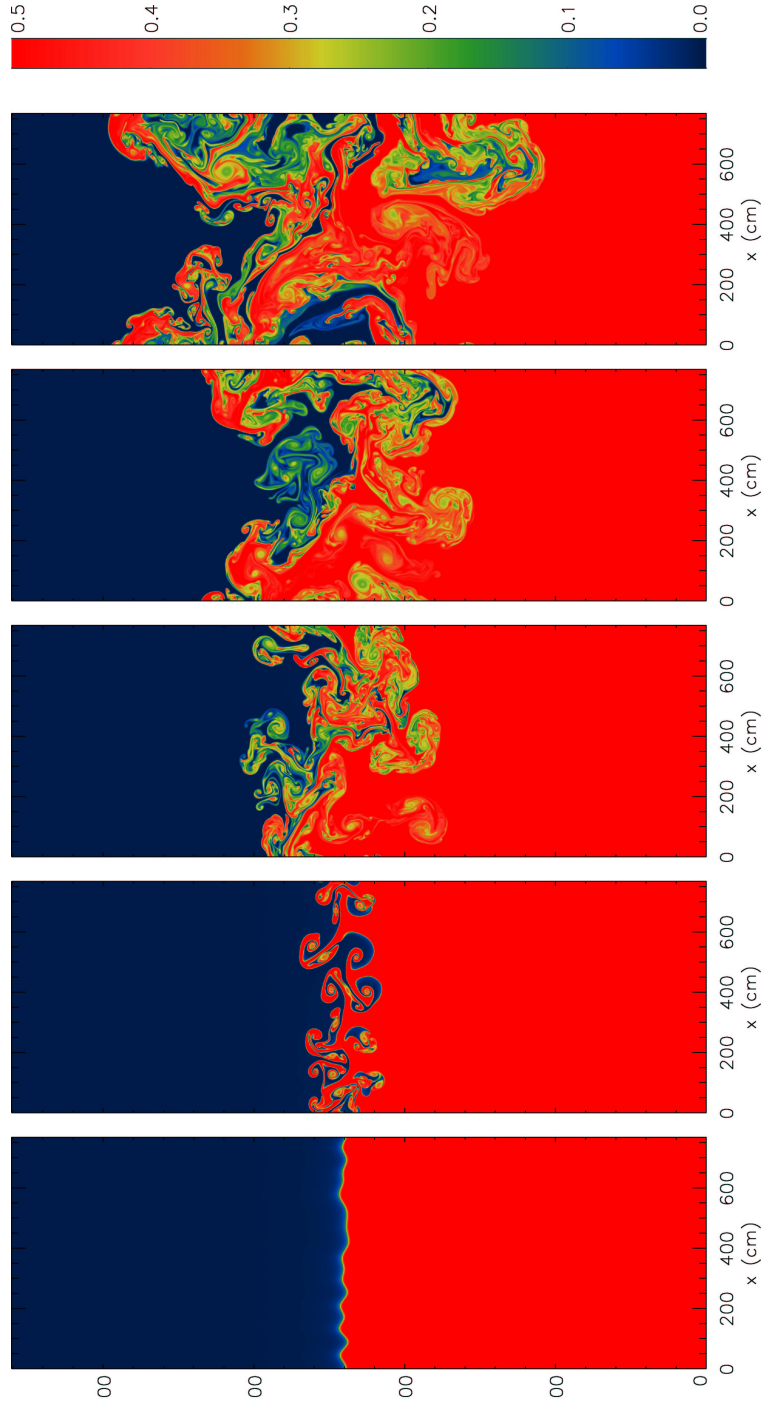
Fig. 1.— Carbon mass fraction for a 768 cm wide, 6.67×10^6 g cm^{-3} C/O flame shown every 1.6×10^{-3} s from 0 s until 6.4×10^{-3} s. The fuel appears red (carbon mass fraction = 0.5), and gravity points toward increasing y. At this low density, the RT instability dominates the burning, and a large mixed region develops. The flame surface is not well defined here, a defining characteristic of the distributed burning regime.
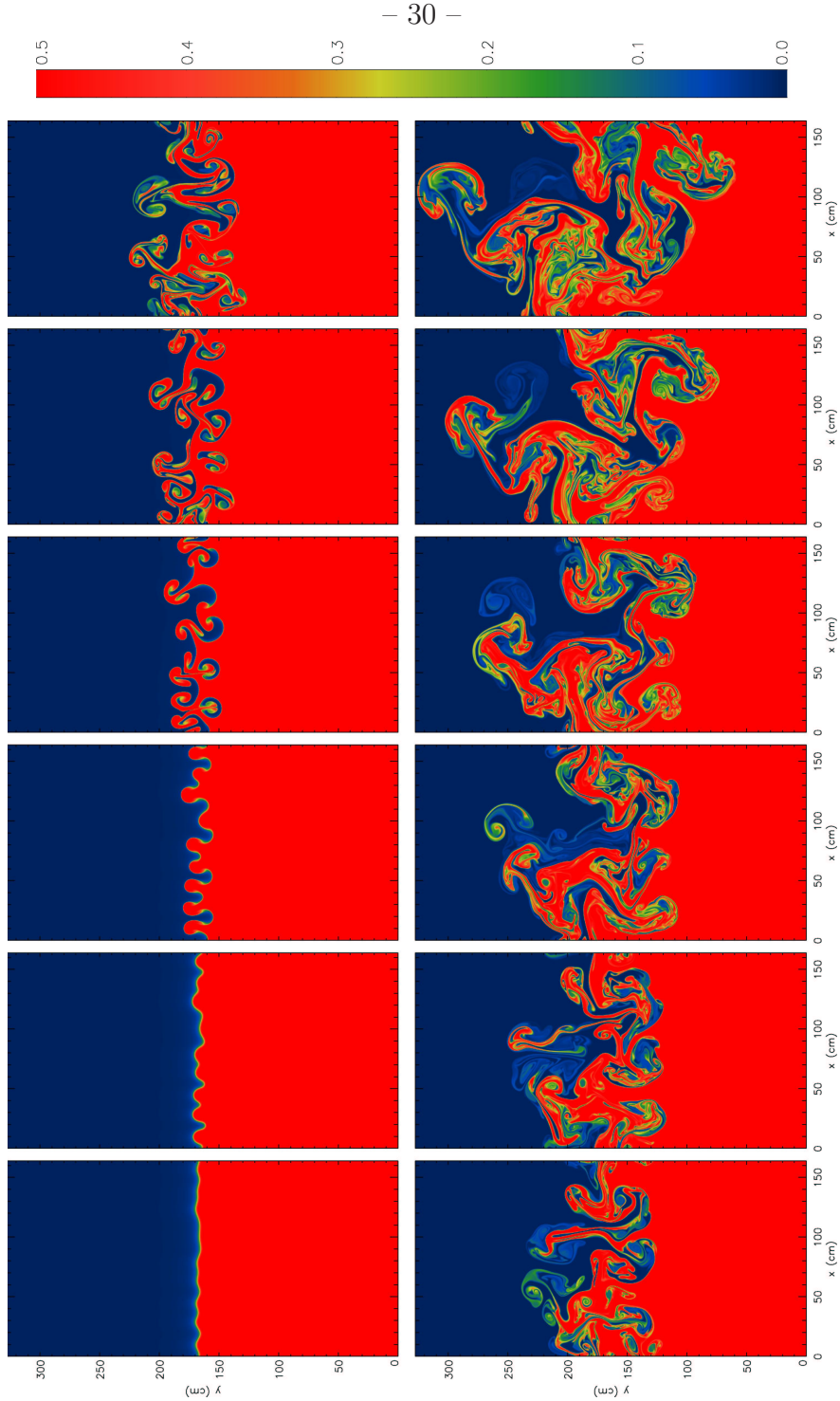
Fig. 2.— Carbon mass fraction for 10^7 g cm^{-3} C/O flame shown every 2.55×10^{-4} s from 0 s until 2.80×10^{-3} s. The fuel appears red (carbon mass fraction = 0.5), and gravity points toward increasing y. As the instability evolves, fingers of denser carbon move into regions of hot ash, and gradually, these fingers burn away, turning yellow and finally blue. The burning and RT growth rate are much better balanced at this density, in comparison to the 6.67×10^6 g cm^{-3} case shown in Figure 1.
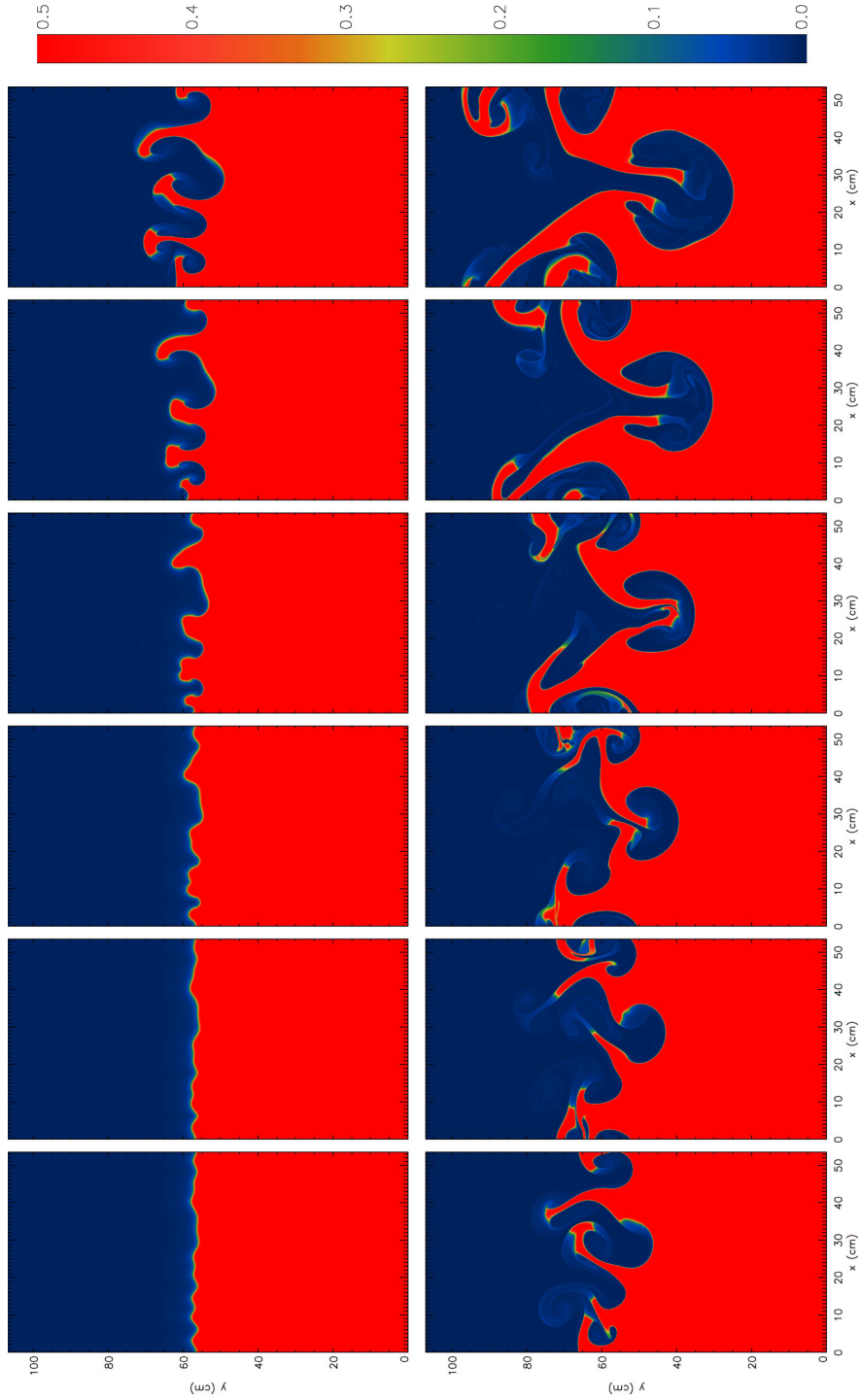
Fig. 3.— Carbon mass fraction for 1.5×10^7 g cm^{-3} C/O flame shown every 1.33×10^{-4} s, from 0 s until 1.46×10^{-3} s. The fuel appears red (carbon mass fraction = 0.5) and gravity points toward increasing y. Here, the burning has a strong effect in moderating the RT instability. In all panels, it is easy to define where the flame front is—there is always a sharp transition from the fuel to ash, a signature of the flamelet regime. This contrasts with the lower density runs, where there is significant mixing.
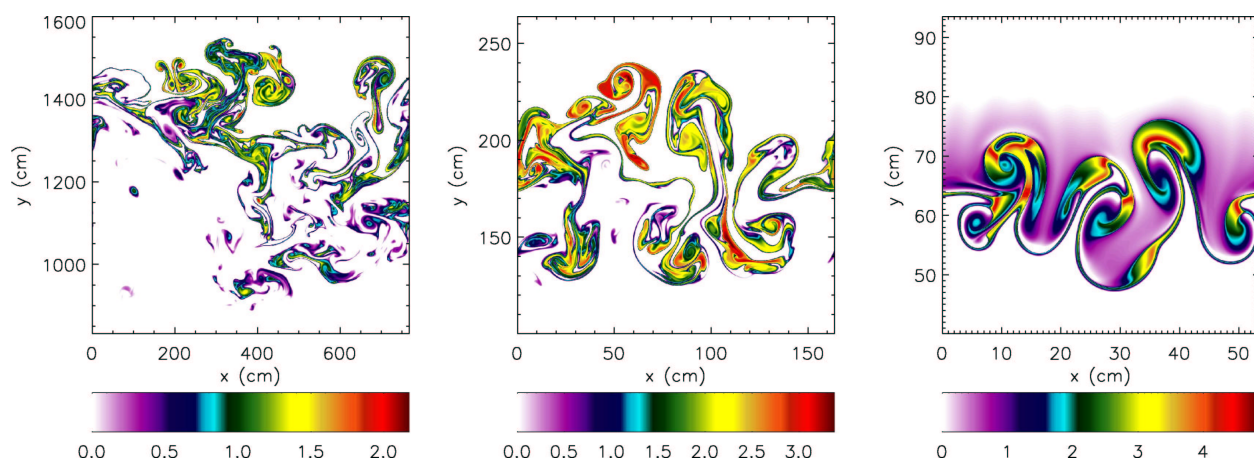
Fig. 4.— Log of carbon destruction rate, $|\dot{\omega}_C|$, for the three densities, 6.67×10^6 g cm^{-3} (left), 10^7 g cm^{-3} (center), and 1.5×10^7 g cm^{-3} (right). The domains are 137, 86.2, and 99.1 flame widths wide respectively. At the lowest density, the peak burning regions are distributed throughout the reactive region in several 'hot' spots. The reactive region becomes more laminar at higher densities, shown here at nearly the same scale in terms of flame widths, as the burning is more effective at curtailing the RT instability.
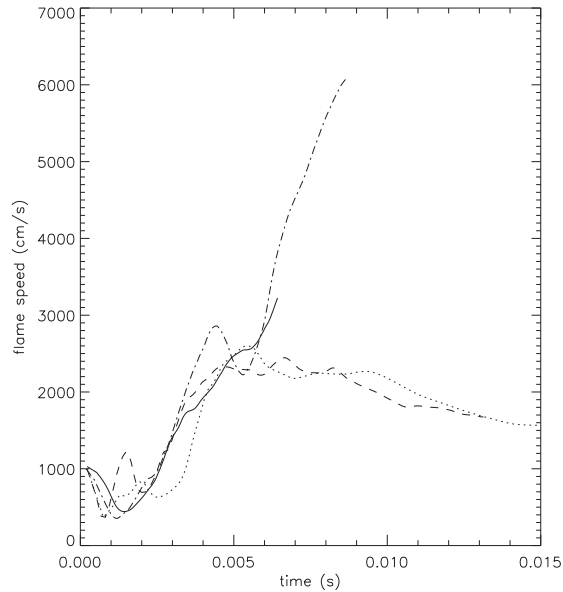
Fig. 5.— Effective flame speed as a function of time for the 6.67×10^6 g cm^{-3} C/O flame RT simulations. The solid line is the main simulation at this density (768 cm wide domain). Also shown are the results from three narrower runs, 384 cm (dot-dash), and 96 cm at high resolution (dashed) and low resolution (dotted)—see Table 2. The peak and asymptotic values of the velocity in the 96 cm domain seem to be insensitive to the resolution, demonstrating convergence. The wider domain allows for longer wavelength modes to go unstable resulting in a larger velocity, as expected.
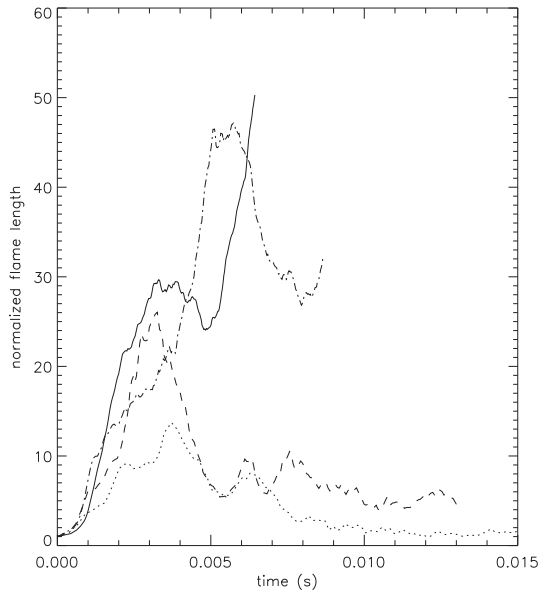
Fig. 6.— Normalized length of the flame, $L(t)/L(t = 0)$, as a function of time for the 6.67×10^6 g cm^{-3} RT simulations. The standard (768 cm wide) case is shown as the solid line. Also shown are three narrower runs, 384 cm wide (dot-dash), and 96 cm wide at high resolution (dashed) and low resolution (dotted). The wider domain allows for longer wavelength modes to grow, leading to the greater increase in flame length as compared to the narrow run. The resolution study shows the finer resolved run producing more area, which is not completely unexpected, given the almost fractal like character of these flames.
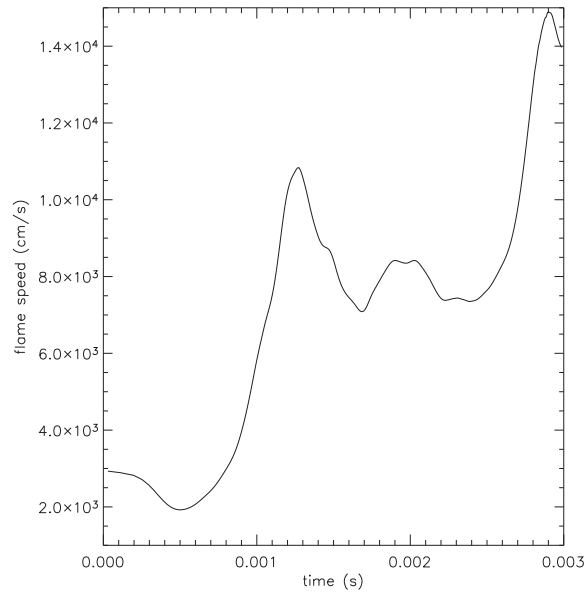
Fig. 7.— Effective flame speed as a function of time for the 10^7 g cm^{-3} RT simulation. Considerable acceleration (factor of 5) is seen as the instability evolves. This run shows no signs of saturating, but is stopped because the spikes of fuel reach the top of the domain.
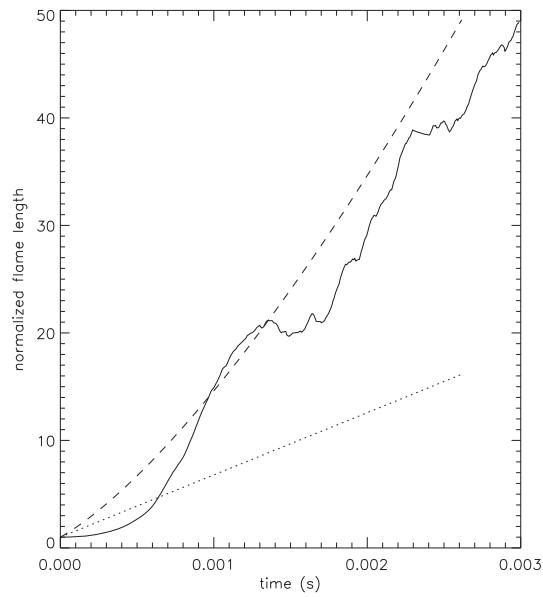
Fig. 8.— Normalized length of the flame, $L(t)/L(t = 0)$, as a function of time for the 10^7 g cm^{-3} RT simulation. Through the course of the simulation, the surface of the flame increases to 50 times its original length. The dotted and dashed lines are predictions from the fractal model for surface growth (Equation [9]), using $D = 1.5$ and $D = 1.7$ respectively. Here, the $D = 1.7$ curve provides a reasonable fit to the numerical data.
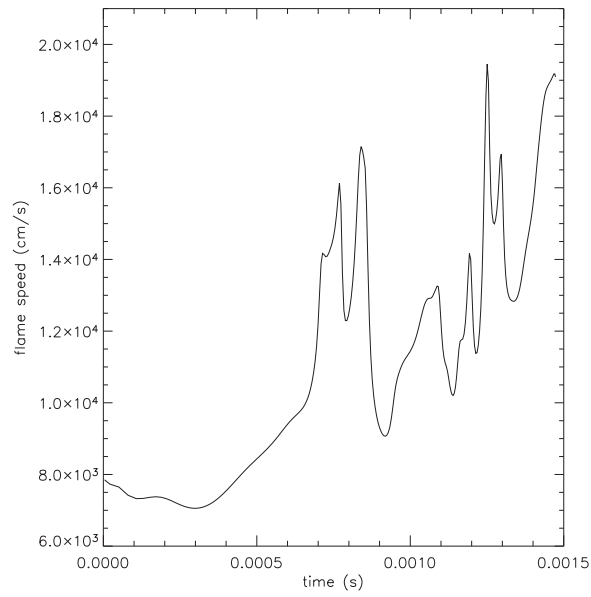
Fig. 9.— Effective flame speed as a function of time for the 1.5×10^7 g cm^{-3} RT simulation. At this density, the velocity is very choppy—reaching a peak and then rapidly falling away as a plume of fuel is consumed, but the overall trend is of increasing velocity, leading to a speedup of about 2.5 times the laminar speed.
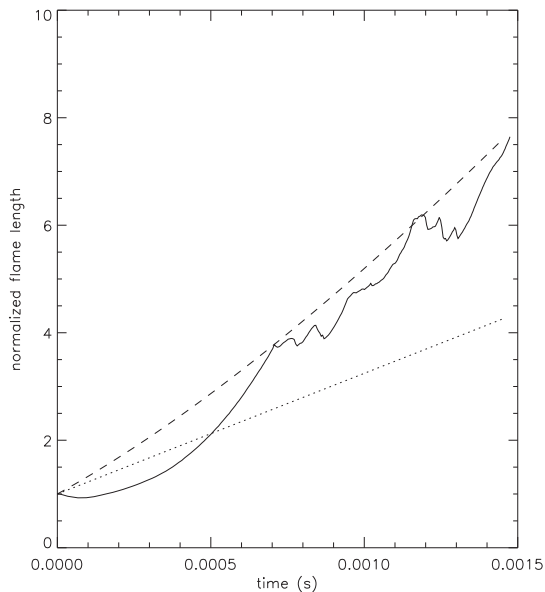
Fig. 10.— Normalized length of the flame, $L(t)/L(t = 0)$, as a function of time for the 1.5×10^7 g cm^{-3} RT simulation. At this density, the growth of the flame length is much smaller than the lower densities (see Figures 6 and 8), reflecting the increased influence of the burning on the RT instability. The dotted and dashed lines are predictions from the fractal model for surface growth (Equation [9]), using $D = 1.5$ and $D = 1.7$ respectively. As in the 10^7 g cm^{-3} case, the $D = 1.7$ curve provides a good fit.
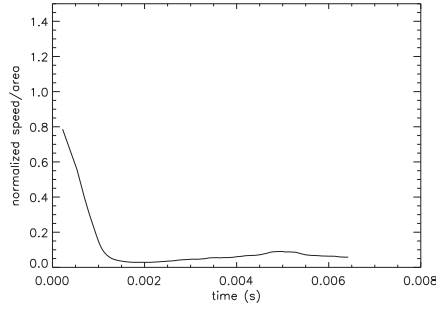
Fig. 11.— Normalized effective flame speed vs. area, $[v(t)/v_{\mathrm{laminar}}]/[l(t)/W]$, as a function of time for 6.67×10^6 g cm^{-3} RT unstable flame in the 768 cm wide domain. Here we see that the speedup is significantly less than the geometrical prediction from the growth in flame surface area.
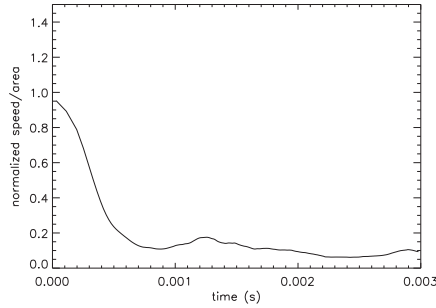
Fig. 12.— Normalized effective flame speed vs. area, $[v(t)/v_{\mathrm{laminar}}]/[l(t)/W]$, as a function of time for 10^7 g cm^{-3} RT unstable flame. Again, we see significant departure from the geometrical prediction for the growth in flame surface area.
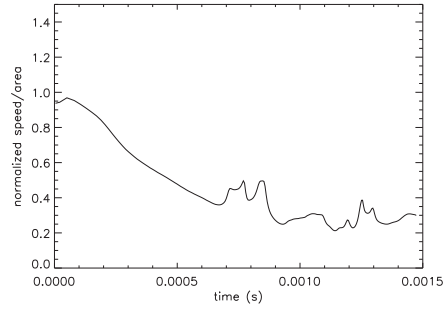
Fig. 13.— Normalized effective flame speed vs. area, $[v(t)/v_{\text{laminar}}]/[l(t)/W]$, as a function of time for 1.5×10^7 g cm^{-3} RT unstable flame. This case is the closest yet to achieving the simple geometrical scaling for the flame speed, but still falls short, asymptoting to about 30% of the geometrical prediction.
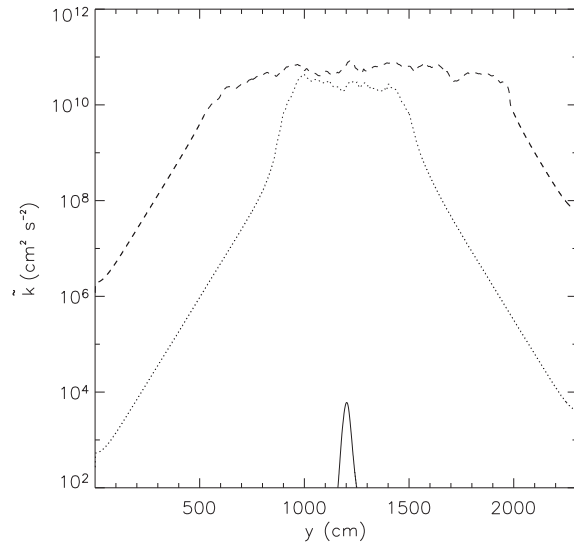
Fig. 14.— Turbulent kinetic energy, $\tilde{k}$, as a function of height for the 768 cm wide 6.67×10^6 g cm^{-3} RT unstable flame three times: 0 s (solid), 3.2×10^{-3} s (dot), and 6.4×10^{-3} s (dash). As the RT flame evolves, the turbulent kinetic energy monotonically increases, with the value roughly constant within the mixed region.
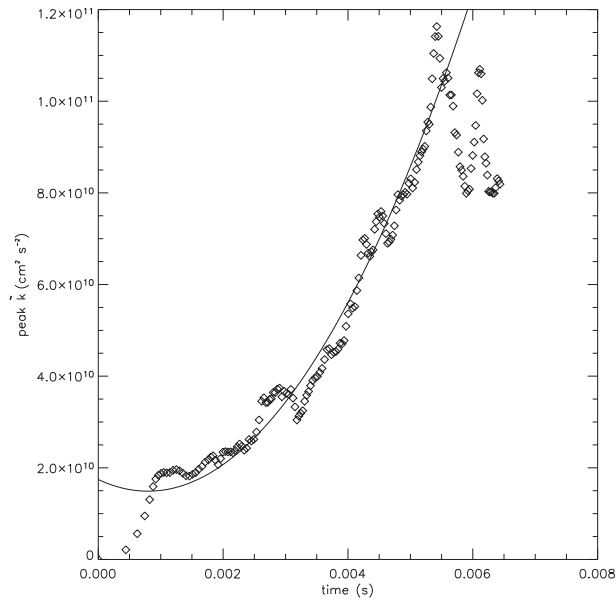
Fig. 15.— Peak turbulent kinetic energy, $\tilde{k}$, as a function of time for the 768 cm wide 6.67×10^6 g cm^{-3} RT unstable flame. The solid line is a quadratic fit to the first 0.0055 s of evolution. At late times, the growth stagnates, as the mixed region becomes larger than the width of the box.
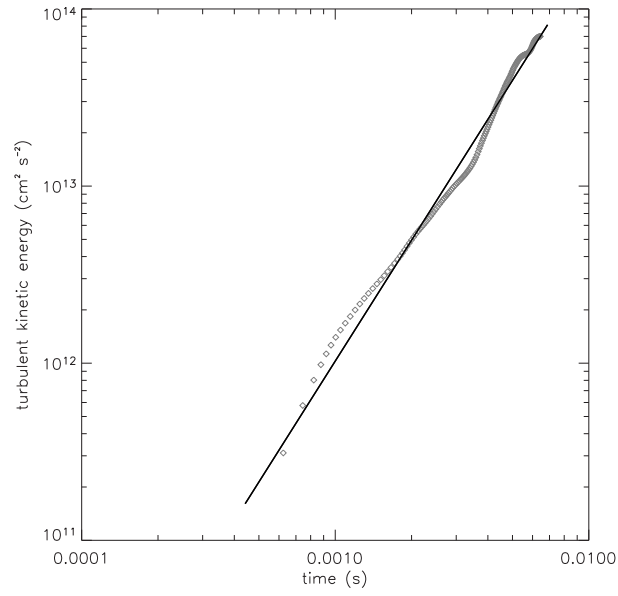
Fig. 16.— Total turbulent kinetic energy as a function of time, $k(t)$, for the 768 cm wide 6.67×10^6 g cm^{-3} RT unstable flame. The symbols are the data and the solid line is a fit, $k(t) = 6.514 \times 10^{18} t^{2.267}$.
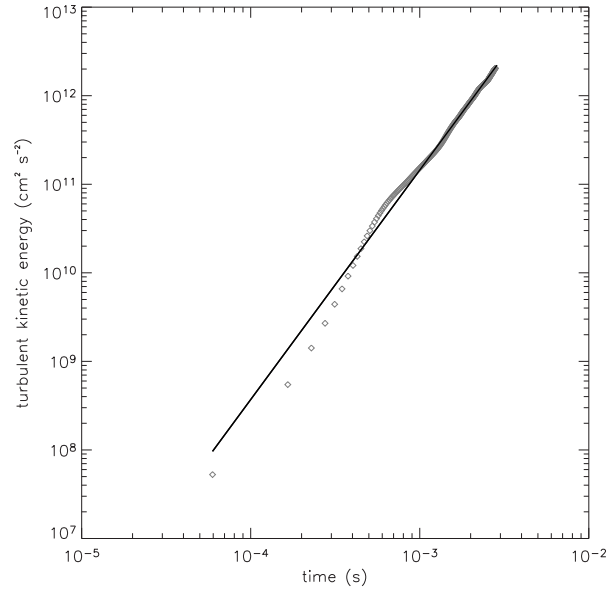
Fig. 17.— Total turbulent kinetic energy as a function of time, $k(t)$, for the 10^7 g cm^{-3} RT unstable flame. The symbols are the data and the solid line is a fit, $k(t) = 8.597 \times 10^{18} t^{2.591}$.
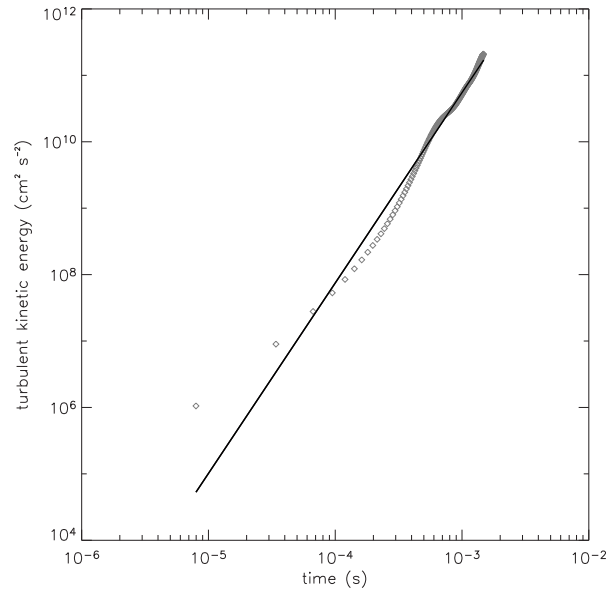
Fig. 18.— Total turbulent kinetic energy as a function of time, $k(t)$, for the 1.5×10^7 g cm^{-3} RT unstable flame. The symbols are the data and the solid line is a fit, $k(t) = 2.202 \times 10^{19} t^{2.867}$.
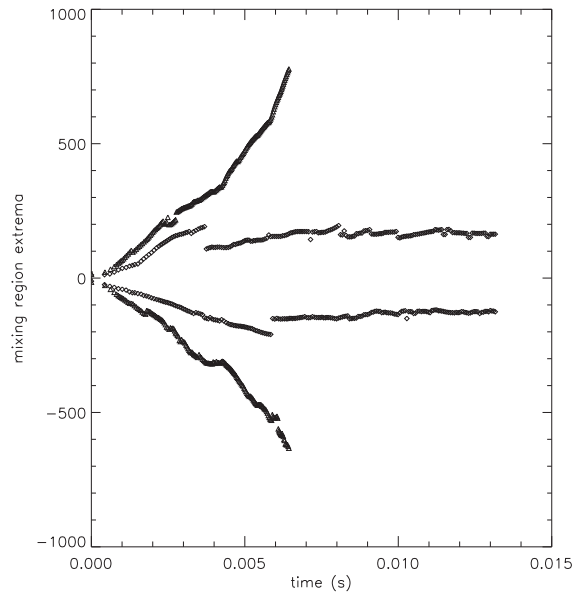
Fig. 19.— Thickness of the mixed carbon region as a function of time for 6.67×10^6 g cm^{-3} C/O flame RT simulation, as measured from the initial position of the interface. '$\diamond$' marks the position in the laterally averaged flame profile where the carbon mass fraction crosses 0.05 and 0.45 respectively for the 96 cm wide domain. '$\triangle$' corresponds to the wider 768 cm domain. We see for the narrow case, the evolution of the flame is halted much earlier, and into a much thinner flame.
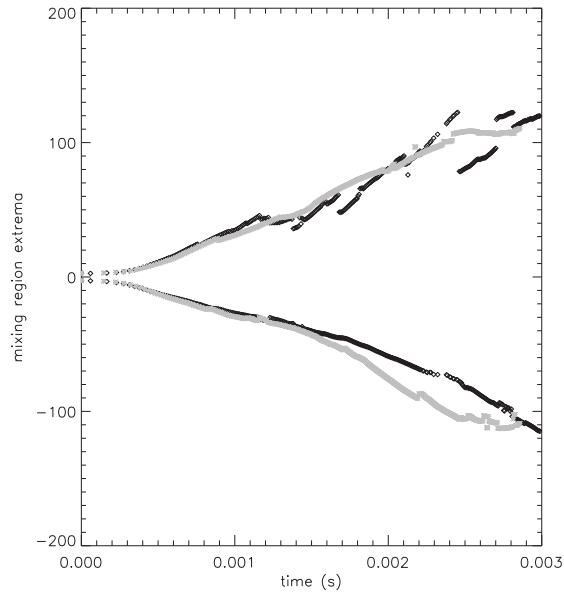
Fig. 20.— Extent of the mixed region as measured from the initial interface for both a reactive and non-reactive 10^7 g cm^{-3} RT simulation as a function of time. Symbols mark the first occurrence of carbon mass fractions of 0.05 and 0.45 in the laterally averaged profiles. The black symbols have burning enabled, whereas the gray symbols have no burning— all other parameters are the same. The effects of burning are immediately clear in this comparison, as the 'no burning' run yields considerably smoother growth curves.
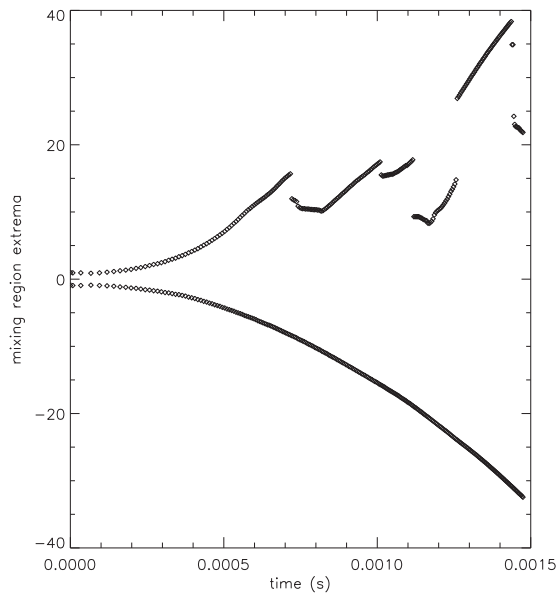
Fig. 21.— Extent of the mixed region as measured from the initial interface for the 1.5×10^7 g cm^{-3} RT simulation as a function of time. Symbols mark the first occurrence of carbon mass fractions of 0.05 and 0.45 in the laterally averaged profiles. The lower curve is the bubble of hot ash pushing into the cool fuel. Because there is nothing to burn away here, it is very smooth, and clearly shows a t^2 behavior.
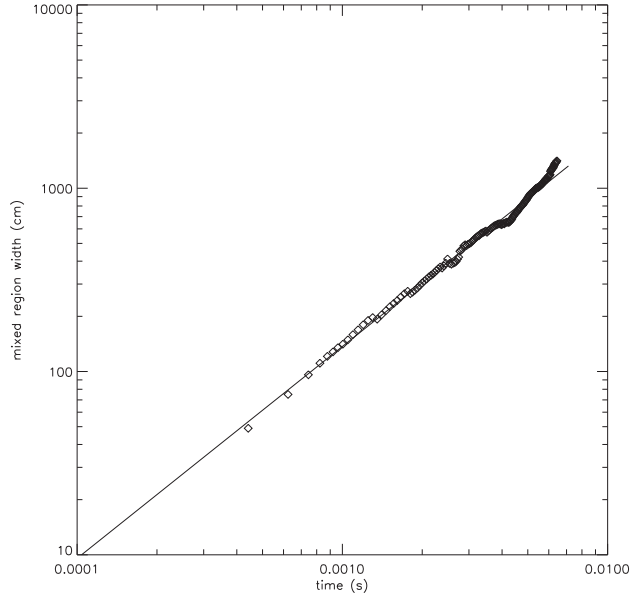
Fig. 22.— Width of the mixed region for the 6.67×10^6 g cm^{-3} RT simulation with a power law fit to time, $w(t) = ct^n$ (solid line), with n = 1.16. The fit was performed over the time interval $[3 \times 10^{-4}$ s, 6×10^{-3} s].
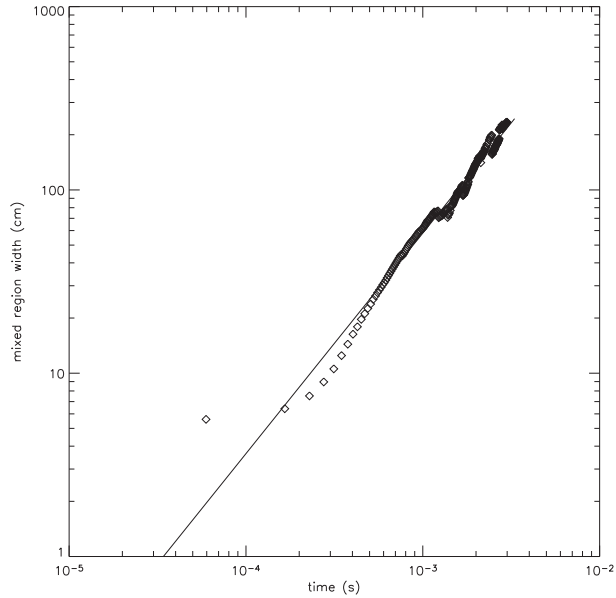

Fig. 23.— Width of the mixed region for the 10^7 g cm^{-3} RT simulation with a power law fit to time, $w(t) = ct^n$ (solid line), with n = 1.2. The fit was performed over the time interval $[5 \times 10^{-4}$ s, 2.8×10^{-3} s].
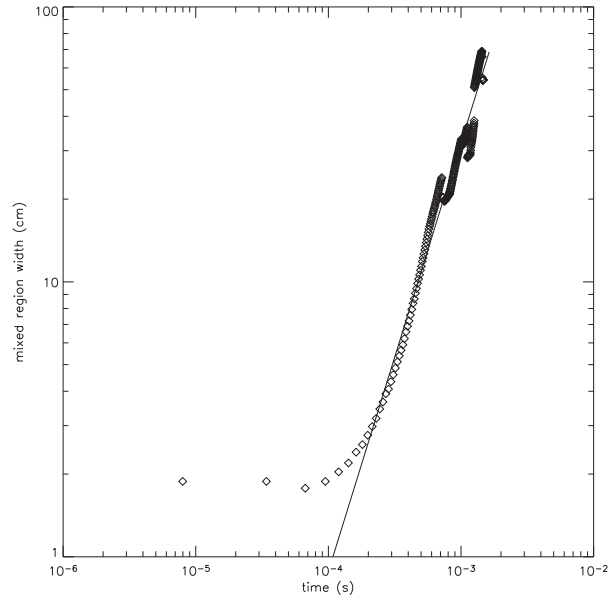
Fig. 24.— Width of the mixed region for the 1.5×10^7 g cm^{-3} RT simulation with a power law fit to time, $w(t) = ct^n$ (solid line), with n = 1.55. The fit was performed over the time interval $[3 \times 10^{-4}$ s, 1.45×10^{-3} s].
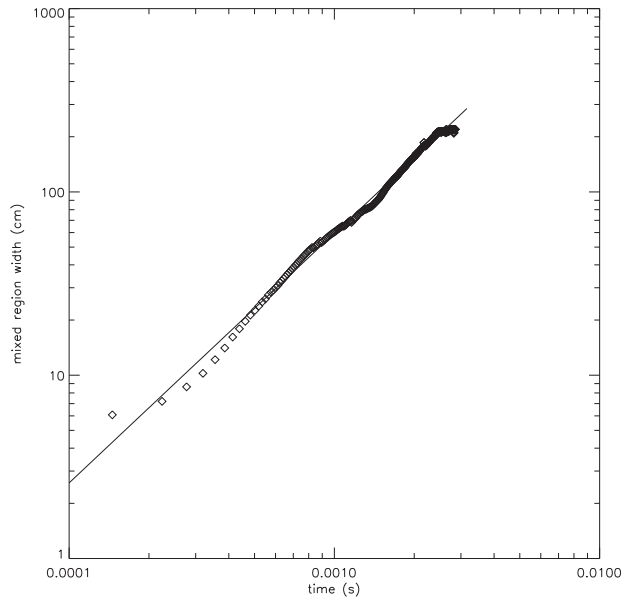
Fig. 25.— Width of the mixed region for the non-reactive 10^7 g cm^{-3} RT simulation with a power law fit to time, $w(t) = ct^n$ (solid line), with n = 1.36. The fit was performed over the time interval $[5 \times 10^{-4}$ s, 2.4×10^{-3} s].
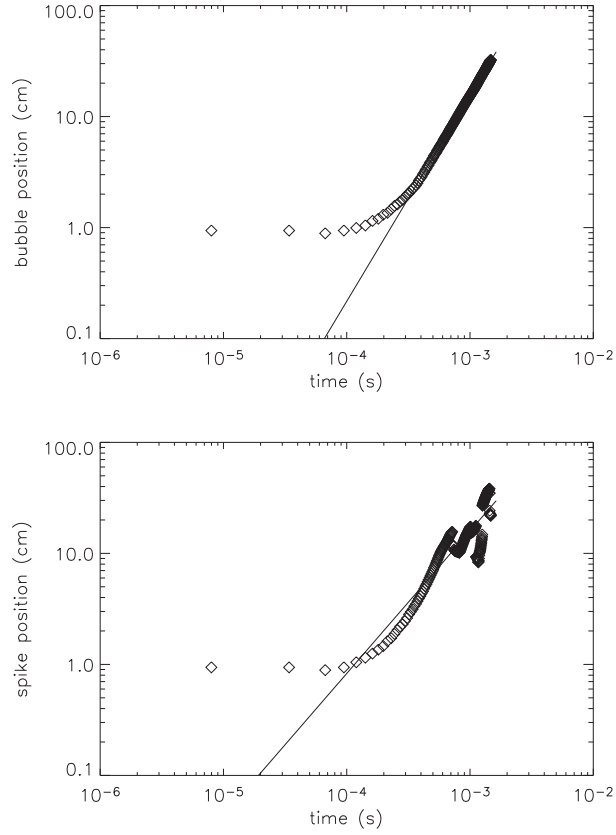
Fig. 26.— Fits of ct^n to the bubble and spike positions for the 1.5×10^7 g cm^{-3} RT run over the time interval $[3 \times 10^{-4}$ s, 1.45×10^{-3} s]. Here we find the bubble position growing with $n = 1.85$ and the spike region growing much slower, with $n = 1.28$. This difference is to be expected due to the strong influence of the reactions burning away the spikes of fuel.
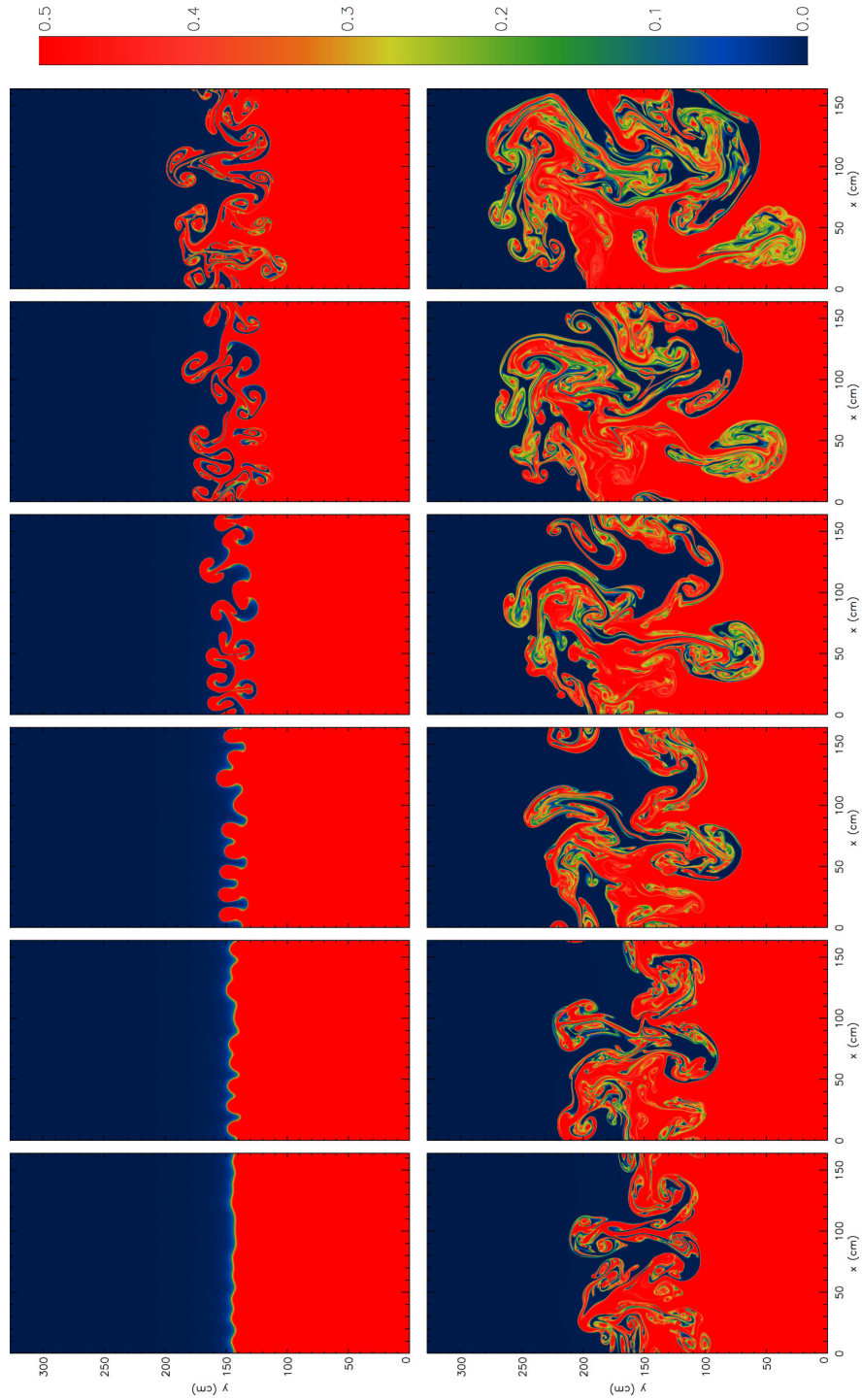
Fig. 27.— Carbon mass fraction for 10^7 g cm^{-3} C/O non-reactive RT simulation shown at the same times as Figure 2. Gravity points toward increasing y.
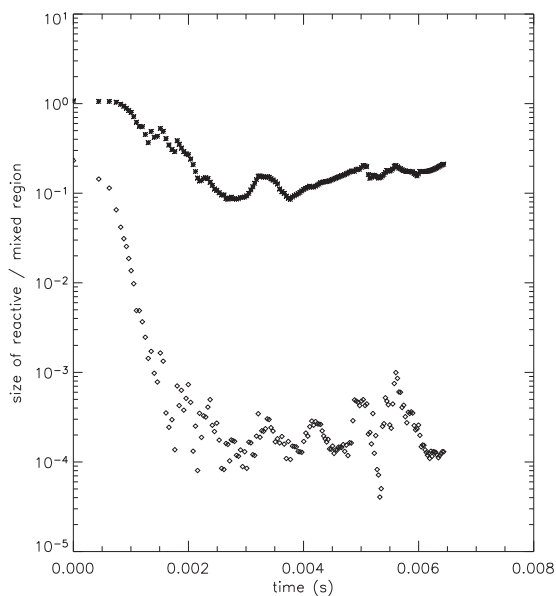
Fig. 28.— Ratio of the size of the reactive region to the mixed region, Γ (see Equation 15), as a function of time for the 6.67×10^6 g cm^{-3} RT unstable flame. Two curves are shown, differing only in the choice of the energy generation rate tolerance, γ (see Equation 14). The '$\times$' are $\gamma = 0.1$ and the '$\diamond$' are $\gamma = 0.8$. After an initial transient, the points appear to level off, indicating that the reactive region grows in direct proportion to the size of the mixed region. The large separation between the two curves, resulting from the strongly peaked nature of the nuclear energy generation rate, does not seem to affect the trend.
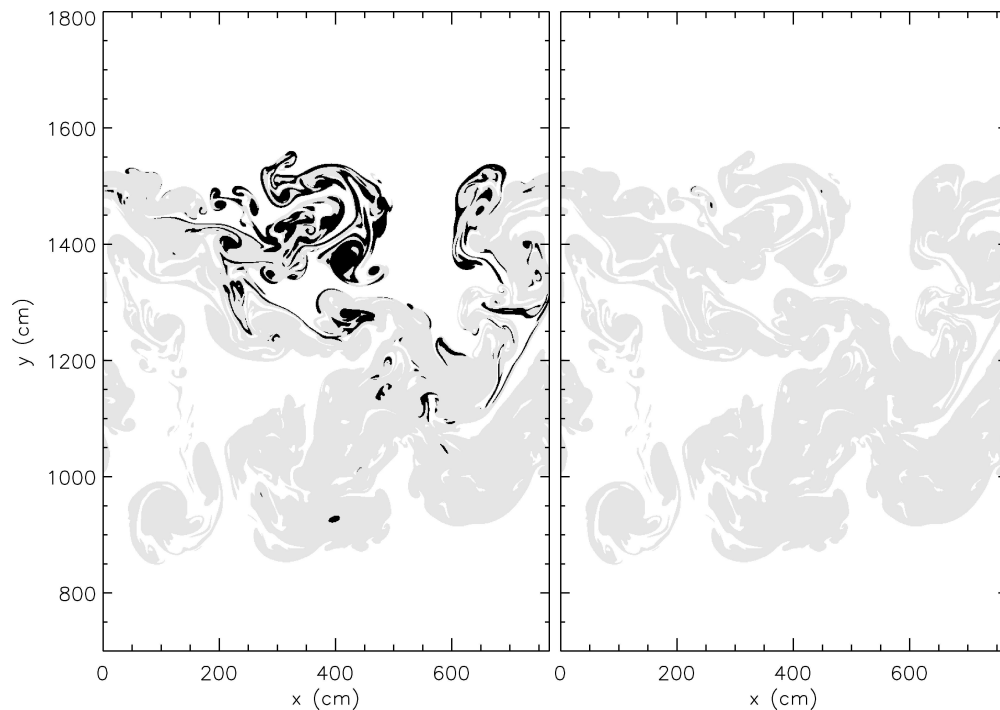
Fig. 29.— Effect of the nuclear energy generation rate threshold parameter, γ, on the relative sizes of the reactive and mixed regions for the 6.67×10^6 g cm^{-3} RT run at 4×10^{-3} s. The mixed region, as defined by Equation 13, appears in gray and the reactive region, Equation 14, is in black, with $\gamma = 0.1$ (left) and $\gamma = 0.8$ (right). Because the reaction rate is strongly peaked, we see a large change in the size of the reactive region between the two panes. This is also reflected in Figure 4. Interestingly, regardless of which value of γ we use, the ratio of the volumes of the reactive region to the mixed region appears to reach a steady state in time (see Figure 28).
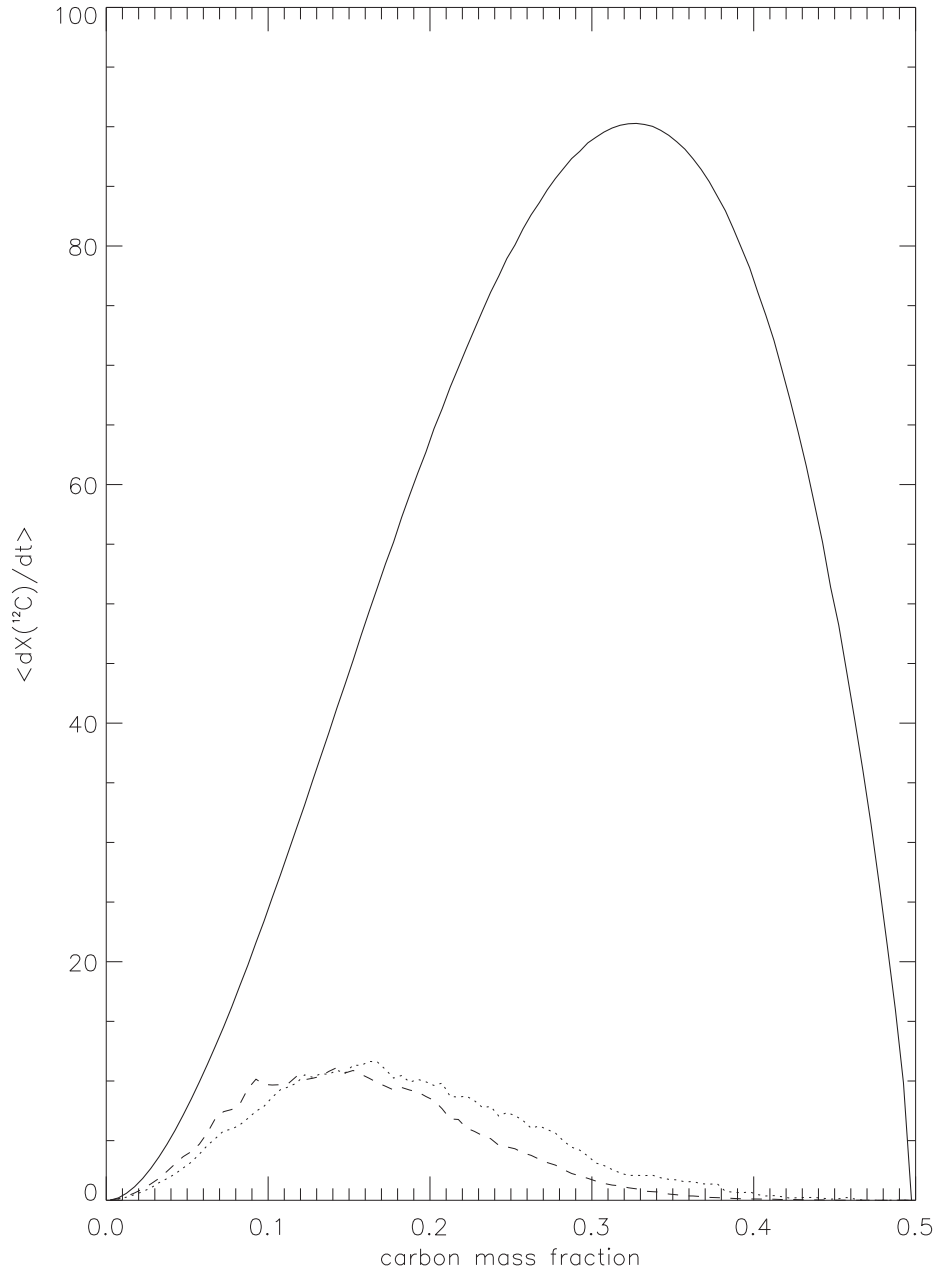
Fig. 30.— Average carbon destruction rate as a function of carbon mass fraction for the 6.67×10^6 g cm^{-3} simulation at 0 s (solid), 3.2×10^{-3} s (dot), and 6.4×10^{-3} s (dash). The average was computed by binning the mass fractions into 100 bins of width 5×10^{-3} and computing the average value of dX_C/dt for all zones whose mass fraction falls in the bin.
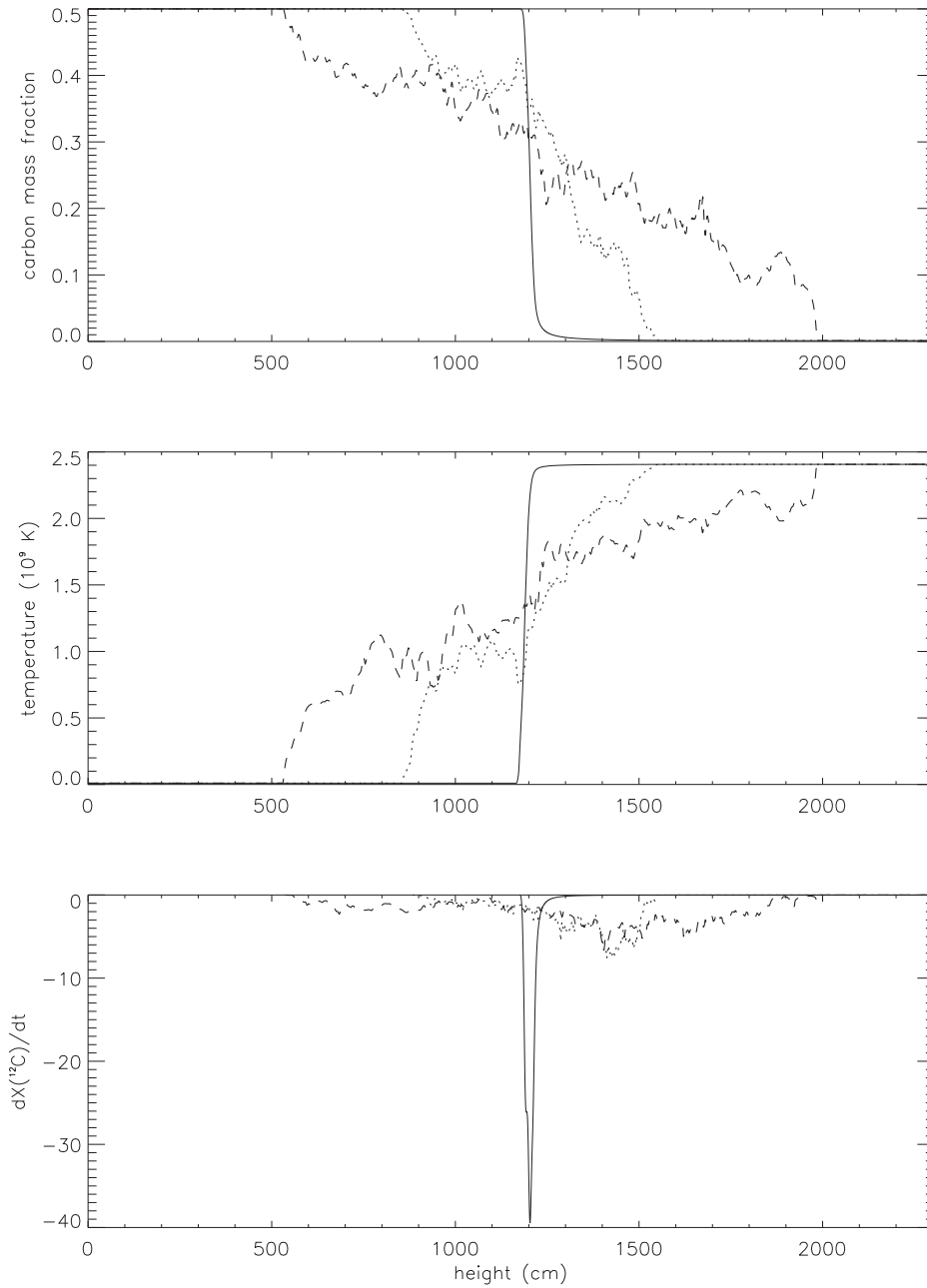
– 56 –

Fig. 31.— Laterally averaged profiles for the 6.67×10^6 g cm^{-3}, 768 cm wide, RT unstable flame showing carbon mass fraction (top), temperature (middle), and carbon destruction rate (bottom), for three times: 0 s (solid), 3.2×10^{-3} s (dot), and 6.4×10^{-3} s (dash). We notice that as time evolves, the 'flame' becomes much broader, and the burning rate sharply decreases. In these figures, the flame is moving to the left.
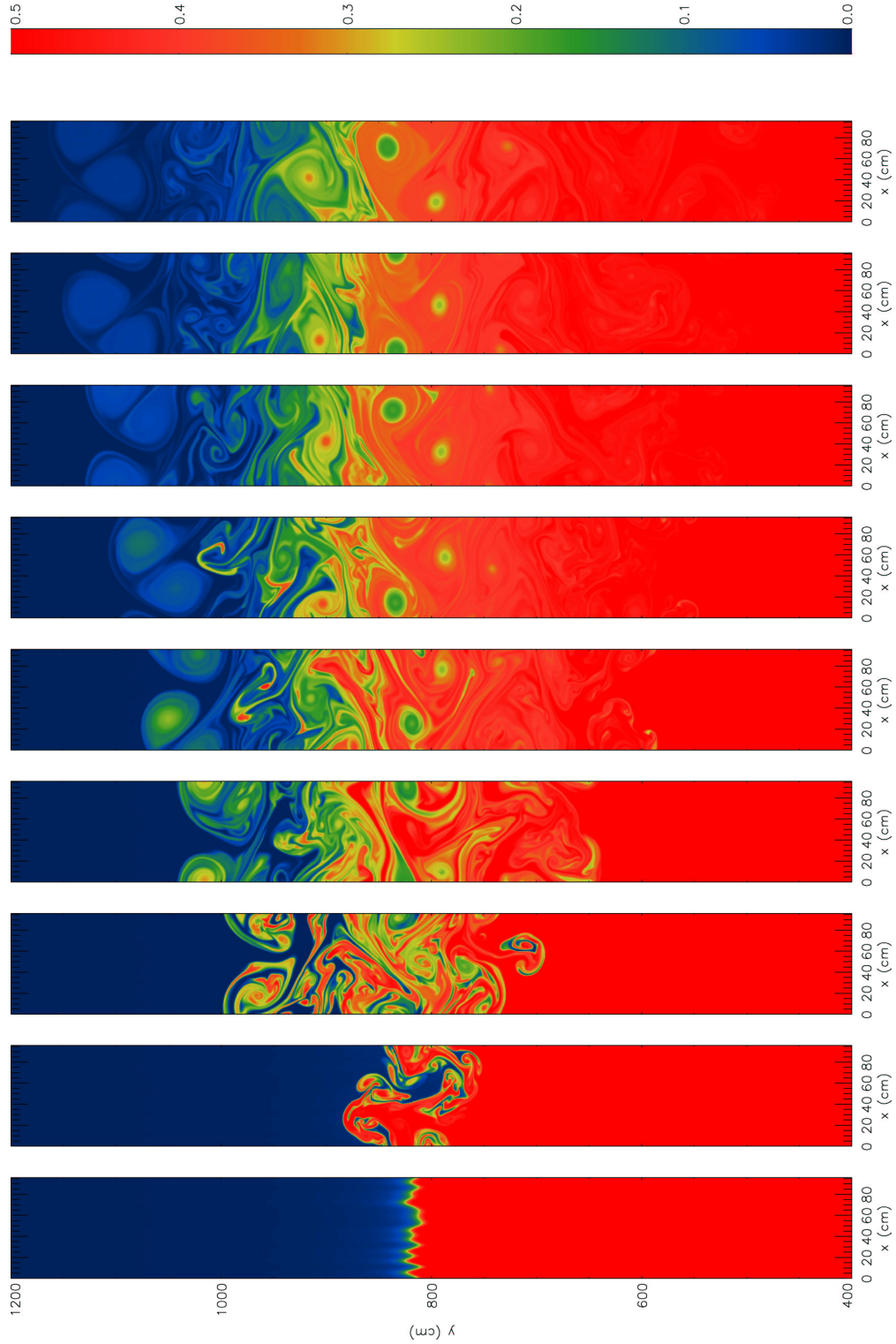
Fig. 32.— Carbon mass fraction for a 96 cm wide, 6.67×10^6 g cm^{-3} C/O flame shown every 1.6×10^{-3} s, starting at 0 s, for the first 1.27×10^{-2} s of evolution. The fuel (0.5 ^{12}C by mass) appears red here and gravity points up. At late times, when the size of the mixed region becomes comparable to the domain width, a steady state shear layer forms, preventing the further growth of the instability.
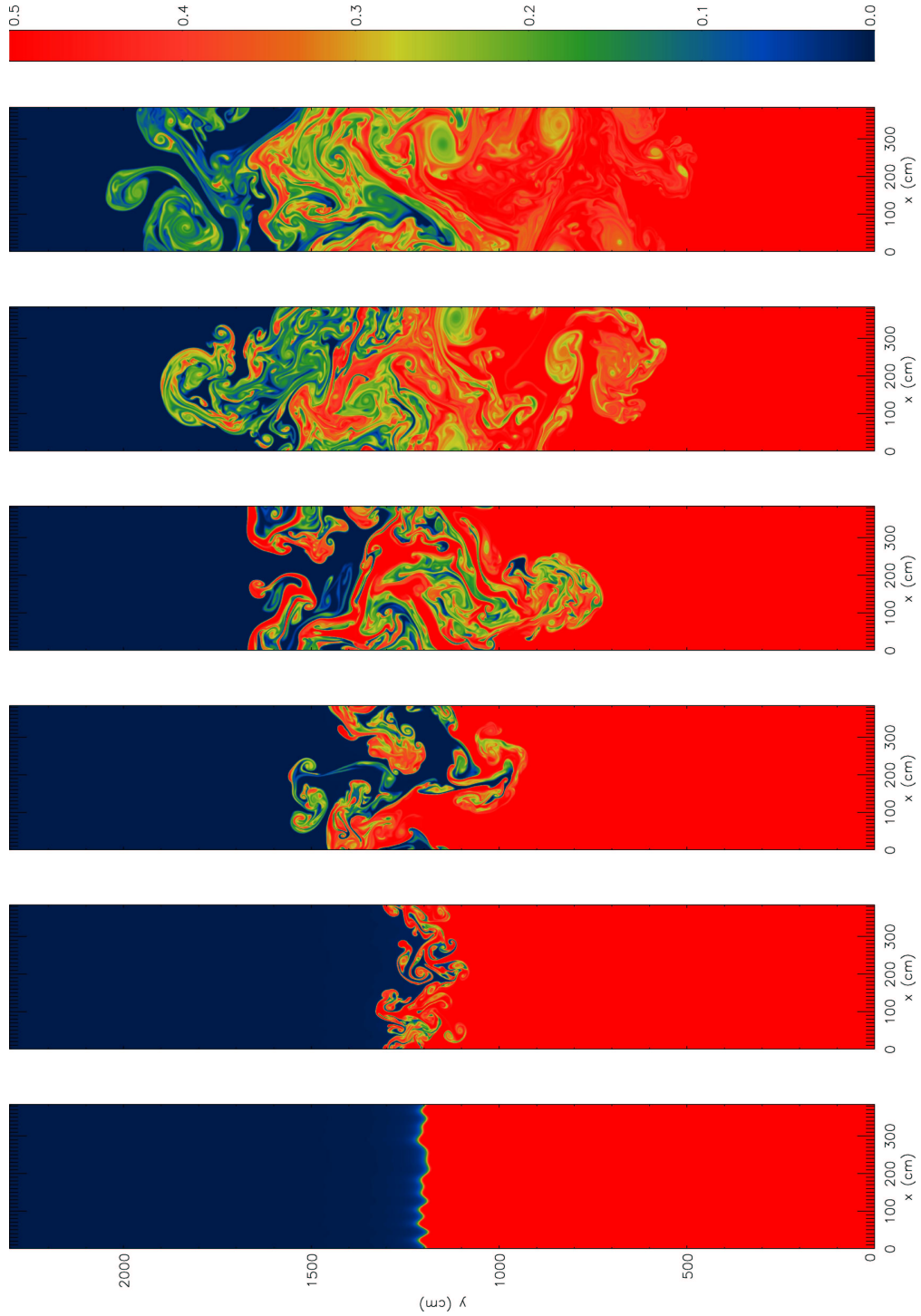
Fig. 33.— Carbon mass fraction for a 384 cm wide, 6.67×10^6 g cm^{-3} C/O flame shown every 1.6×10^{-3} s until 8.12×10^{-2} s. The fuel appears red (carbon mass fraction = 0.5), and gravity points toward increasing y. At this low density, the RT instability dominates over the burning, and a large mixed region develops.
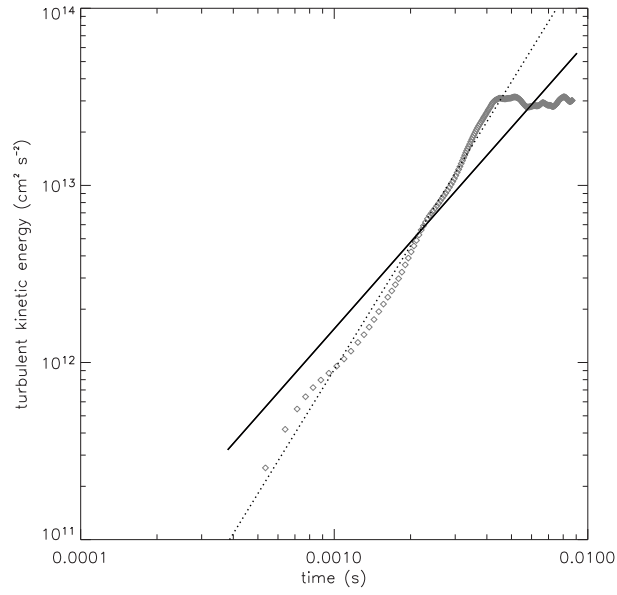
Fig. 34.— Turbulent kinetic energy as a function of time for the 384 cm wide 6.67×10^6 g cm^{-3} RT unstable flame. The symbols are the data and two fits are provided. The solid line is all the data, $k(t) = 1.169 \times 10^{17} t^{1.626}$. The dotted line is just the initial 0.005 s, the period up to the point where the mixed region grows to rival the domain wide in extent, and gives $k(t) = 8.602 \times 10^{18} t^{2.325}$. This latter fit agrees well with the wider domain results, Figure 16.